

This is an Open Access document downloaded from ORCA, Cardiff University's institutional repository: <https://orca.cardiff.ac.uk/id/eprint/166020/>

This is the author's version of a work that was submitted to / accepted for publication.

Citation for final published version:

Cukur, Deniz, Um, In-Kwon, Buchs, David M. , Kim, Seong-Pil, Kong, Gee-Soo, Chun, Jong-Hwa, Horozal, Senay, Hong, Seok-Hwi, Yu, Shin and Kim, Tae-Yeon 2024. Submarine landslides on the Eastern South Korea Plateau (ESKP) - Do pumice-rich tephra layers control slope stability? *Marine Geology* 467 , 107205. 10.1016/j.margeo.2023.107205

Publishers page: <http://dx.doi.org/10.1016/j.margeo.2023.107205>

Please note:

Changes made as a result of publishing processes such as copy-editing, formatting and page numbers may not be reflected in this version. For the definitive version of this publication, please refer to the published source. You are advised to consult the publisher's version if you wish to cite this paper.

This version is being made available in accordance with publisher policies. See <http://orca.cf.ac.uk/policies.html> for usage policies. Copyright and moral rights for publications made available in ORCA are retained by the copyright holders.



Submarine landslides on the Eastern South Korea Plateau (ESKP) - Do pumice-rich tephra layers control slope stability?

Deniz Cukur^{1*}, In-Kwon Um¹, David M. Buchs², Seong-Pil Kim¹, Gee-Soo Kong¹, Jong-Hwa Chun¹, Senay Horozal³, Seok-Hwi Hong¹, Shin Yu¹, Tae-Yeon Kim¹

¹Petroleum and Marine Research Div., Korea Institute of Geoscience and Mineral Resources (KIGAM), 124, Gwahak-ro, Yuseong-gu, Daejeon 34132, Republic of Korea

²School of Earth and Environmental Sciences, Cardiff University, UK

³Chungnam National University, Dept. of Oceanography and Ocean Environmental Sciences, Daejeon 34132, Republic of Korea

Corresponding author: Dr. Deniz Cukur

Email: dcukur@kigam.re.kr

Abstract

Tephra layers embedded in marine sediments can be significant in controlling submarine landslide dynamics and seafloor morphology, but their preconditioning effects on slope failure remain uncertain. Here, we study the morphology and preconditioning factors of submarine landslides from a volcanically active region, the Eastern South Korea Plateau (ESKP) using a recently acquired multibeam echosounder (MBES), high-resolution sub-bottom chirp profiler, and piston core data, together with previous geophysical data. At least 50 translational landslides were identified on the southern margin of the ESKP in an area of $\sim 470 \text{ km}^2$, with a relatively small volume of remobilized sediment ($\sim 10 \text{ km}^3$). The landslide headscarps are arcuate, up to 400 m in height, and lie at water depths of 980 to 2300 m. Landslides on the upper ESKP margin are more disintegrative (debris flow type) than those on the lower margin which consists largely of blocky type failures with small runouts. Landslide deposits identified in the cores consist of debris flows and slides/slumps while background deposits contain hemipelagic mud interbedded with ca. 10-cm-thick coarse-grained, poorly-sorted pumiceous tephra. Seismic and core integration indicate that the glide planes of the observed slides correspond to the pumice-rich tephra layers. These tephra are predominantly composed of fresh volcanic glass devoid of clay, indicating that the composition of the tephra did not control the formation of weak layers or slide planes. We infer therefore that the weakness of the glide planes resulted from high hydraulic (pore)

pressure at the interface between some of the porous tephra layers and their overlying, relatively impermeable, hemipelagic mud. In addition to burial compaction and build-up of pore pressure in the tephra layers, fluid overpressure could have been facilitated by earthquakes causing granular convection within, and compaction of, the poorly sorted tephra. The landslide predominantly formed > ca. 84 ka ago, which suggests time-restricted triggering associated with a temporary increase in seismicity and/or sediments reaching their overpressure threshold during burial compaction. Our study suggests that regional occurrences of discrete layers of porous tephra deposits within finer grained hemipelagic sediments can potentially control the generation of landslides in subaqueous environments affected by explosive volcanism.

Keywords: submarine landslides, tephra layers, piston cores, Eastern South Korea Plateau

1. Introduction

Submarine landslides and resulting sediment gravity flows are the dominant processes for sediment transport from continental shelves to the deep oceans (Talling et al., 2012), which can damage or destroy seabed infrastructure and generate destructive tsunamis (Hampton et al., 1996; Masson et al., 2006). However, although submarine landslides are widespread and destructive, the physical processes that precondition or trigger submarine slope failures remain little understood. This is mainly due to the high cost of (1) comprehensive in situ geotechnical investigations and (2) sampling landslide deposits by deep drilling techniques such as the Ocean Drilling Program (Piper et al., 2012). Moreover, it is difficult to monitor or record submarine landslides on the ocean floor because they are episodic (Talling et al., 2012).

Many studies have suggested that submarine landslides are triggered by earthquakes and other short-term phenomena (i.e., large storms) (Hampton et al., 1996). However, long-term preconditioning factors, including tectonic steepening, fault location and geometry, dissociation of methane hydrates, elevated subsurface fluid pressures caused by high sedimentation rates, fluid flows, and changes in sea level, can all exert a crucial role in causing slopes to fail (Hampton et al., 1996; Masson et al., 2006; Camerlenghi et al., 2010, and references therein). In particular, the occurrence of so-called *weak layers* embedded within the slope stratigraphy is suggested to control the localization of submarine landslides and their failure planes (e.g., Masson et al., 2006; L'Heureux et al., 2012; Locat et al., 2014; Gatter et al., 2021).

Volcaniclastic layers are commonly presumed to have a high liquefaction susceptibility and have been suggested as weak layers of many submarine landslides (Harders et al., 2010; Sassa et al., 2012; Strasser et al., 2012; Laberg et al., 2014; Kuhlmann et al., 2017; Sammartini et al., 2019; Gatter

et al., 2021). For example, in a study of the Hermosa slide offshore Costa Rica, Harders et al. (2010) proposed that the rearrangement and breakage of elongated ash particles, e.g., due to seismic shaking, may cause a sudden volume reduction that promotes a rapid accumulation of pore fluid at the interface between ash beds and overlying clay-rich sediments. This water-rich veneer abruptly reduces shear strength, creating a glide plane for translational sliding. Similarly, a coarse-grained ash layer containing sub-angular pumice and glass shards overlain by clayey sediments has been identified as a potential failure surface of the Licosa Slide, offshore southwestern Italy (Sammartini et al., 2019). The permeable ash likely enabled lateral fluid flow along the layer. In contrast, the work of Wiemer and Kopf (2015, 2017) from South-Central Chile suggests that hard-grained ash sands (low crushability) may actually increase the shear strength of the slope material due to the particles' roughness and angularity, favouring seismic strengthening. Soft-grained pumice, however, may also be weak due to its high crushability, thus favouring pore pressure build-up in sedimentary deposits (Wiemer and Kopf, 2017). Alternatively, many previous studies (Hyodo et al. 1998; Orense et al. 2014; Orense and Pender 2015; Asadi et al. 2018; de Cristofaro et al. 2022) have shown that crushable, volcanically-derived soil (e.g., pumice, tephra) exhibits a higher liquefaction resistance than similar non-crushable materials. Previous studies of MTDs in volcanically active margins therefore agree that the unique mechanical and hydraulic characteristics of tephra layers interbedded within marine sediments can be significant in controlling landslide dynamics, but the exact preconditioning effects of these layers on slope failure remain poorly understood. This study provides additional constraints on this issue and submarine landslide dynamics using a new dataset from the Eastern South Korea Plateau (ESKP), which is a volcanically active region marking the transition between the Eurasian continental margin and the East Sea (Japan Sea) back-arc basin. The study area includes widespread occurrence of mass-transport deposits (MTDs), tephra layers, and faults that offer an ideal opportunity to further constrain processes that precondition or trigger slope failure and ultimately control the submarine morphology of volcanically active regions.

The primary objectives of this study are to (1) document the morphology of the submarine landslides in the ESKP; (2) integrate high-resolution sub-bottom chirp profiler data and sediment cores to assess internal characteristics of MTDs and surrounding sediments, including deformation style, pore pressure, and the presence of gas; (3) integrate the high-resolution sub-bottom chirp profiler data with existing IODP borehole data farther up the slope to document the timing of MTDs and nature of glide planes in which landslides initiated; and (4) investigate possible subsurface triggers and precondition factors for MTDs, including the role of tephra layers on slope failures..

2. Geological and physiographic setting

The study area is located in the East Sea, along the southern margin of the South Korea Plateau (SKP), in close vicinity to Ulleungdo and Dokdo volcanic islands as well as several large volcanic seamounts (Fig. 1). The SKP formed in response to back-arc extension and rifting of continental crust

that began in the early Oligocene (ca. 32 Ma) in the northeastern Japan Basin, and was locally followed by seafloor spreading since the late Oligocene (ca. 28 Ma) (Tamaki et al., 1992). Continued crustal extension in the East Sea formed the Yamato and Ulleung Basins that border the SKP (Tamaki et al., 1992). A plate reorganization in the middle Miocene along eastern and southeastern Japan caused crustal shortening and back-arc inversion, resulting in a series of thrusts and anticlines in the southern margin of the Ulleung Basin (Lee et al., 2011).

The East Sea comprises several deep-water (>1,000 m) marginal plateaus separated by narrow and deeper (>3,000 m) topographic basins (Fig. 1). Of these, the SKP forms one of the largest continental fragments in the rift basin, with an estimated crustal thickness of 15 km (Kim et al., 2015). The SKP is divided into the western (WSKP) and eastern (ESKP) parts by the North Ulleung Trough which is 20 km wide and 100 km long. The ESKP, which is the focus of our study, ranges in width from 260–350 km and covers an area of approximately 11,000 km² (Horozal et al., 2017). It is bounded by the Ulleung Basin in the south, the Ulleung Interplain Gap (a basin ~90 km long and over 2500 m deep) in the southeast, the Japan Basin in the north, and the N-S- trending North Ulleung Trough in the west.

The Ulleung Basin lies in water depths of over 2000 m with a smooth seafloor disrupted by Ulleungdo Volcano and Anyongbok Seamount in the north, and Dokdo Volcano and flat-topped seamounts in the northeast (Fig. 1). The Ulleungdo Volcano is the largest active volcanic feature in the study area, which rises ~2100 m above the seafloor and forms a 73 km² island. This active volcanic island is believed to be the source of several beds of alkaline (trachytic to phonolitic) tephra that were deposited throughout the East Sea during the Quaternary (Arai et al., 1981; Machida and Arai, 1983, 1988; Chun et al., 1997, 2007; Park et al., 2003, 2007; Shiihara et al., 2013; Ikehara, 2015; Lim et al., 2013; Chen et al., 2018). Tephra from Ulleungdo volcano has been reported as far as central Onshu, Japan (e.g., McLean et al., 2020). The Anyongbok seamount is a conical volcanic edifice that rises ~1600 m above the seafloor to a depth of ~2100 m. The flanks of the seamount are replete with large-scale morphological features such as flank cones and flank rift zones (Kang et al., 2007). Recent dredging and geochemical analyses of igneous rocks have shown that the seamount is compositionally similar to Ulleungdo Volcano with an assemblage of alkaline products, including trachybasalt and basanite to trachyte and phonolite lavas and volcanoclastic deposits (Choi et al., 2022). An age of 1.74 ± 0.01 Ma was obtained by the ⁴⁰Ar/³⁹Ar method on a dredged phonotephrite (Choi et al., 2022), but there is no evidence of more recent or active volcanism at this seamount. Dokdo Volcano and nearby flat-topped seamounts northeast of Ulleung Basin are erosional remnants of older volcanoes (Kim et al., 2013; Choi et al., 2022; Park et al., 2022), with volcanism at Dokdo active between approximately 4.6 and 1.6 Ma (Park et al., 2022, and references therein). The age of volcanic activity at these older volcanoes predates the age of deposition of surficial seafloor sediments and tephra sampled in our study.

Site U1430 of the Integrated Ocean Drilling Program (IODP) Expedition 346 provides the only

well control on the southern upper slope of the ESKP adjacent to our study area (Tada et al., 2015) (Fig. 1). Three drill holes were drilled at Site U1430, with a maximum depth of 275 m below the seabed. Shipboard observations show that Site U1430 is dominated by pelagic and/or hemipelagic biogenic sediments with minor volcanic (tephra) and terrigenous (clay to sand) input since the Miocene (Tada et al., 2015). Major lithological changes at Site U1430, such as alternating centimeter- to meter-scale of dark and light layers, are inferred to reflect local and eustatic sea-level changes, climate oscillations, and volcanic and diagenetic processes in the East Sea (Tada et al., 2015).

More recent structural and stratigraphic constraints on the evolution of the ESKP was provided by Horozal et al. (2017), which builds upon previous regional interpretations (e.g., Kim et al., 2015) using an integration of regional seismic reflection profiles and borehole data at Site U1430 from IODP Expedition 346. Regional seismic reflection profiles reveal that the ESKP comprises a series of NE-trending basement highs and grabens and half grabens with sediment thicknesses of ~1.5 km. The sedimentary succession in the depocentres is dominated by Late Oligocene and Middle Miocene syn-rift clastic sediments, overlain by Late Miocene to Recent post-rift hemipelagic-pelagic sediments (Horozal et al., 2017). A number of major unconformities were also identified by Horozal et al. (2017), which correspond to significant tectonic events (typically uplift, inversion, and erosion), and bound the major seismic megasequences. These deformation events seem mostly correlated with regional tectonic events in the SW East Sea (as described above), with a local overprint by smaller-scale rift-related deformation. Overall, the sedimentary changes in the ESKP are inferred to have been chiefly controlled by regional/local tectonics with the secondary influence of regional climatic and paleo-oceanographic processes including significant eustatic changes in the Pliocene-Quaternary (Horozal et al., 2017).

3. Datasets and methods

Data used in this study include: (1) approximately 600 km of 3.5 kHz sub-bottom chirp profiles collected by the Korea Institute of Geoscience and Mineral Resources (KIGAM) in 2020 and 2021 (Fig. 1B); (2) multibeam echosounder (MBES) data acquired by the KIGAM from 2020 to 2021 for the “Development of Integrated Geological Information Based on Digital Mapping” project; (3) five piston cores collected by KIGAM in 2020 and 2021 to a maximum depth of 7.70 mbsf (Fig. 1B, Table S1); (4) non-destructive measurements of physical properties on the archived (split) core sections; (5) point magnetic susceptibility measurements on the archived (split) core sections; (6) IODP drill data farther up the slope from Holes U1430A, U1430B, and U1430C (Tada et al., 2015) to enable core seismic integration and age correlation; and (7) major element compositions of four coarse-grained pumice samples using X-ray Fluorescence Spectrometer (XRF) to determine their source and composition (Table 1).

The sub-bottom chirp data were acquired using an SYQWEST-BATHY 2010 sub-bottom

profiler system. The chirp system provides a signal penetration of up to 60 m with a vertical resolution of ~8 cm. We used IHS Kingdom Suite® software to interpret chirp seismic reflection data and to integrate seismic and core data. Data interpretation included the following steps: (1) identification of the seismic facies and their interpretation to infer lithofacies; and (2) mapping key seismic horizons and their correlation to IODP drill Site U1430 to constrain their lithology and age. We correlated high-resolution chirp seismic and core data by using P-wave velocities from Hole U1430A to convert depth in the drill hole to two-way travel time.

MBES data were collected using a hull-mounted Kongsberg EM 302 and processed by Caris HIPS/SIPS software with a horizontal resolution of 50 m. We used Global Mapper® software to analyze the MBES data. A number of steps were used to map the landslide-affected areas. The first step was the identification of headwall scarps from the shaded relief and slope maps derived from the bathymetric data. Second, using shaded-relief bathymetry, the areas affected by landslides were outlined by polygons that encompass the region of negative elevation within the landslide's headwall and sidewalls. Third, the volume of each landslide was calculated using a method similar to ten Brink et al. (2006), in which a smooth upper surface interpolated from the polygon that defines the boundary of each failure scar and is then subtracted from the extracted bathymetric data (lower surface) within a global mapper (Chaytor et al., 2009). Finally, the statistics of landslide parameters (i.e., volume, length, width, headwall slope, height, slope angle, etc.) were calculated and cross-plotted to infer their interrelationships.

The piston cores were recovered in and outside of slide scars; two cores (20MAP-P15 and 21MAP-P08A) were sited below the headwall scar, and three-piston cores (20MAP-P16, 21MAP-P06, and P11) were collected outside of the scars (Fig. 1B; Table S1). X-ray radiographs of 1-cm-thick sediment slabs (25-cm-long) were taken from one-half of the split cores to define the sedimentary structures. Subsamples were taken for grain size analysis using a laser particle size analyzer (Microtrac S3500). Samples were treated with hydrogen peroxide to remove organic material and then with a dilute solution of hydrochloric acid to remove carbonates. After rinsing thoroughly with distilled water, the sample was placed in an ultrasonic bath for up to 2 mins to break up any remaining aggregates before being analyzed by the laser particle size analyzer. To facilitate the comparison between primary volcanoclastic and sedimentary deposits we applied the clastic sediment grain size terminology to all deposits irrespective of their origin; this approach has little practical inconvenience considering that the grain size subdivision of clastic sediments is used to name primary volcanoclastic deposits (White and Houghton, 2006). Digital images of core surfaces were obtained using a line-scan camera, and color-reflectance values (L^*) profiles were deduced from the other half of the image of the split core. Undrained shear strengths were measured at the KIGAM laboratory using a vane shear at increments of approximately 10 cm. Shear strength values are reported for hemipelagic fine grained sediments.

For the non-destructive measurements of physical properties, a multi-sensor core logger (MSCL) from GEOTEK Ltd at KIGAM was used to measure gamma-ray attenuated (GRA) bulk density at 1 cm increments. For the major element compositions of pumice samples, the pumices were separated and cleaned with deionized water, before crushing to powder for whole-rock geochemical analysis. The analytical totals of our results and reference datasets from previous studies were normalized to 100 wt% before plotting and interpretation.

4. Results

4.1 Morphology and distribution of submarine landslides

At least 50 submarine landslides were identified with MBES data along the southern margin of the ESKP (Fig. 2A–B; Table S2). Overall, landslide scarps have an arcuate shape morphology (e.g., Fig. 3A–C) with some having rectangular shapes on the lowermost ESKP margin (i.e., SL36; Fig. 3D). The landslide headwall scarps range in water depth from 980 m at the highest observed headwall scarp to 2,337 m at the lowest observed headwall scarp. The arcuate-shaped headwall scarps range in height from 5 m to 400 m (mean: 115 m; Fig. 4A), in width from 0.5 km to 11 km (mean: 2.5 km; Fig. 4B), and dip from 2° to 30° (mean: 15°; Fig. 4C). The dip and height of headwall scarps increase towards the lower ESKP margin (Fig. 4A and C). The average dip angle on which landslides have occurred is 2.2° and 5.2° on the upper and lower ESKP margin, respectively (Fig. 4D). The largest estimated volume of mobilized sediment is about 1.2 km³ while the smallest one is 0.001 km³ (Fig. 4E). In total, an estimated 10 km³ of sediment has been mobilized in the study area due to sediment mass failures. The area affected by individual landslides ranges from 1 to 38 km², summing to 470 km², representing approximately 20% of the studied ESKP seafloor (Fig. 4F).

The relationship between landslide parameters was investigated in the upper, middle, lower, and lowermost ESKP margin (Fig. 5A–D). Although weak ($R^2=0.3$), there is an inverse correlation between the landslide length (i.e., runout) and the slope angle (Fig. 5A). The coefficient of determination increases to $R^2=0.4$ when outliers are removed from the correlation. The smallest runout landslides occur on the steep slopes of the lower margin, whereas the longest runout landslides occur on more gentle slopes of the upper margin. Some landslides have the longest length of slope failure (i.e., SL1, 9, 10, 13, 14, and 28) at a given slope angle in the source area and some of these (i.e., 9 and 13) have also a very high headwall height, and are located in close proximity to faults (Fig. S3).

A plot of headwall height against slope angle shows a positive correlation ($R^2=0.3$ without outliers) for all regions, with only a few outliers (Fig. 5B). Headwalls of failures tend to be lower on low slope angles and increase with higher angles. Outliers in the middle (SL9 and SL13) and lower (SL4, 5, and 7) slopes are mostly distinct from outliers observed in the slope angle vs slope angle trend. These landslides have taller scarps and are usually located along faults (Fig. S3). There is also a well-

constrained positive correlation between scarp dip and slope angle ($R^2=0.4$), showing increasing angles with water depth (Fig. 5C).

The variability in the slope angle in the source area is correlated to the water depth ($R^2=0.3$), with also an increase in the slope angle with water depth (Fig. 5D). Here there are no fault-controlled outliers as the water depths are independent of the faults.

4.2 Acoustic evidence of landslides

One of the shallowest scarps discovered in the area, measuring about 20 m in height, is shown in Fig. 6A-B. Strata downslope of the scarp are characterized by transparent seismic reflections interpreted as mass-transport deposits (MTDs; See also next section Sedimentary Facies). Strata upslope of the scarp yield moderate- to high-amplitude parallel, continuous reflections, representing undisturbed ESKP margin sediments consisting of alternations of hemipelagic deposits and tephra layers (See next section Sedimentary Facies). The base of the MTDs, representing the glide plane, is characterized by a high amplitude continuous reflection, parallel to the ESKP margin stratigraphy. Profiles both parallel (Fig. 6A) and perpendicular to (Fig. 6B) scarp indicate that landslide deposits vary in thickness from 7 m to as much as 13 m and extend as far as 17 km from the base of the scarp into the adjacent basin floor. Based on the areal extent and thickness of the disturbed zones observed from MBES and chirp seismic data it is estimated that about 0.1 km^3 of sediment was affected during this failure. Faulting and internal stratigraphical deformation can be observed on reflection profiles at the edges of the disturbed zones.

Another chirp seismic profile traversing the lower part of the slope region is shown in figure 6C. The sequence downslope of the scarp shows transparent seismic reflection characteristics of MTDs. Where not disturbed by landslides, the seismic sequence yields moderate- to high-amplitude parallel continuous reflections. Coring investigations from these parallel reflectors indicate that these strata consist of hemipelagic sediments interbedded with pumice-rich tephra layers (see next section Sedimentary Facies). A series of lower scarps and adjacent unfailed sediment blocks can also be observed from high-resolution chirp profiles.

Chirp seismic profiles crossing unfailed ESKP margin areas further image past sediment mass failures in the study area. Chirp seismic profile (Fig. 6D), for instance, shows a ca. 14 m thick MTD unit that is internally characterized by transparent seismic reflections. Cores recovered from this MTDs unit show highly disturbed sediment, representing debris flow and slumped material (see next section Sedimentary Facies). The overlying parallel continuous reflections that drape the MTDs are represented by hemipelagic sediments and tephra layers also observed in the cores.

Chirp seismic profiles (Fig. 7A-D) traversing the submarine landslides SL 41, SL 42, SL 38,

and SL 36 clearly show headwall scarps and associated MTDs below the scarps. Chirp seismic profiles also show some different types of landslide deposits in the upper and lower ESKP margin. Chirp seismic profiles on the lower ESKP margin (Figs. 7C and 7D), for example, show hyperbolic reflections which are typical for slides/slumps. In contrast, on the upper slope, they show wedge-shaped transparent seismic reflections which are diagnostics for the debris flows. Moreover, chirp seismic profiles from the deep basinal areas do not show any evidence for MTDs (Fig. 7D). A prominent seafloor fault can also be seen immediately above the headwall scarp of SL 36 (Fig. 7D).

4.3 Sedimentary characteristics and physical properties

4.3.1 Sedimentary facies

The piston core sediments are divided into five sedimentary facies based on lithological changes and sedimentary structures: bioturbated mud (BM), crudely laminated mud (CLM), mud clast mud (MCM), deformed mud (DM), and tephra layers (T) (Figs. 8A and S1).

The BM facies is by far the most abundant, consisting of mud with mottling and pyrite filaments of variously shaped burrows (Fig. 8A). The coarse fraction of these facies is principally composed of planktonic and benthic foraminifers (Fig. 8B), diatoms and radiolarians (Fig. S2A), quartz and feldspar (Fig. S2B), lithic fragments (Fig. S2B), plant fragments (Fig. S2C), elongated mineralized burrow molds (Fig. S2D), and volcanic clasts including pumice granules (Fig. S2E) and smaller volcanic glass shards (Fig. S2F).

The CLM (crudely laminated mud; encompassing ~2 % of the individual core lengths) facies is characterized by continuous horizontal laminae that often include abundant planktonic foraminifers (Figs. 8A-8C). The facies units are generally 8-28 cm thick and have sharp lower and gradational upper boundaries. The BM and CLM facies closely resemble those described by Bahk et al. (2000) in the Ulleung Basin and are of inferred hemipelagic origin under well- to poorly oxygenated bottom-water conditions.

Facies MCM (mud clast mud) consists of mud clasts of varying shapes, sizes, and colors (Fig. 8A). Mud clasts are supported by a muddy matrix and are angular to subrounded. Clasts are <1 to > 8 cm in diameter and exhibit well-defined boundaries. The upper and lower contacts between MCM facies and the underlying and overlying hemipelagic facies (BM) are relatively sharp. Compositionally, the sand fraction of facies MCM includes foraminifers, diatoms, plant fragments, and volcanic fragments (Fig. 8D). Facies MCM occurs only at core P08A (~227-316 mbsf). This facies unit is interpreted as mass-transport deposits (i.e., debris flow deposits) in accordance with previous studies (Damuth and Olson, 2015; McHugh et al., 1996).

Facies DM (deformed mud) represents deformed mud layers that appear to be contorted or

folded, tilted, and inclined (Fig. 8A). The matrix of facies DM deposits is primarily composed of sandy silt and silt. The coarse-grained components of the DM facies constitute planktonic and benthic foraminifers, quartz, and wood fragments (Fig. 8E). Intervals of DM facies that show contorted or folded beds are interpreted as slumps (McHugh et al., 1996). The less-deformed intervals that contain tilted or inclined beds are interpreted as slides.

Tephra layers (T) are interbedded in hemipelagic deposits and are common throughout the cored sediment samples (Figs. 8A and S1). Tephra layers are used here in the sense of explosively-erupted, unconsolidated, pyroclastic products of a volcanic eruption of any grain size or composition (Lowe, 2011), whereas pumice is defined as volcanically-derived vesicular, lightweight glass-shard particles (e.g., Chaneva et al. 2023). Pumiceous particles can occur in every grain size (fine ash to lapilli). The pumiceous tephra layers are fresh, white to gray in color (dominantly white; Fig. 8F, G, H, and I), less than 1 cm to 10 cm thick, and consist mainly of silt to granule (see next section). Smaller volcanic shards are preferentially found in the thinner tephra layers (Fig. 8J). Many pumiceous tephra layers include mm-sized lithic fragments (Fig. S2H) that are associated with higher magnetic susceptibility (see section 4.3.3).

4.3.2 Provenance and identification of tephra layers

The four analyzed tephra layers have very similar petrography with abundant rounded to subrounded pumice grains (sand to granule in size) and minor lithics and euhedral volcanic minerals (typically feldspar with subordinate amphibole and mica). The pumices have trachytic and phonolitic compositions, with $\text{SiO}_2 = 61.68\text{-}60.81$ wt%, $\text{K}_2\text{O} = 5.65\text{-}5.99$ wt%, and $\text{Na}_2\text{O} = 7.91\text{-}9.43$ wt% (total alkali = 13.89-15.08 wt%) (Fig. 9; Table 1). These compositions closely match those of tephra from Ulleungdo volcano found on Ulleung island and surrounding marine sediments (Fig. 9; e.g., Shiihara et al., 2011). The composition of the pumices is also similar to the most differentiated igneous rocks dredged on the flanks of Ulleung island and Dokdo seamount (Choi et al., 2022). The analyzed tephra beds are clearly distinct from lesser alkaline to subalkaline tephra layers erupted from Baekdusan and Japanese volcanoes, which also have higher TiO_2 at a given SiO_2 content (Fig. 9B).

A distinctive, up to ~10 cm-thick tephra layer occurs in all drilled cores (Figs. 8F and G; Fig. S1), which provides a useful stratigraphic marker in the study area; pumices of these layers yielded similar Ulleungdo-like compositions in two analyses (samples 20MAP-P15 (30-32 cm) and 20MAP-P16 (116-119 cm; Table 1). Based on its stratigraphic position, this bed is tentatively interpreted as the U-Sado tephra layer (sensu Lim et al., 2013), also known as the SKP-II layer (Chun et al., 2007). U-Sado layer is a distinctive tephra with an Ulleungdo compositional affinity, which occurs predominantly in the East Sea to the SE of Ulleungdo volcano (Arai et al., 1981), and which was previously cored on the southern ESKP close to the study area (Chun et al., 2007). Reverse grading of pumices described

by Chun et al. (2007) has also been observed in our cores. The depositional age of this layer has been considered ca. 60-61 ka based on regional stratigraphic constraints (Lim et al., 2013) and the age model from the Oki Ridge, located about 300 km further E-SE of the study area (Chun et al., 2007). The recurrence and spatial extent of the several other (unnamed?) tephra layers with Ulleungdo geochemical affinities seen in our cores remains to be studied.

4.3.3 Composition, grain size, and sorting

The fine-grained hemipelagic sediments from all piston cores have a typically muddy composition (medium to fine silt) with the average grain diameter for each core falling within silt sizes of 5 to 7 phi (Fig. 10A). In contrast, samples from interbedded tephra layers exhibit the coarsest grain-size distribution in all the cores, with median size ranging from 0.4 phi to 2.5 phi (coarse- to fine-sand). Grain size distributions indicate that most fine-grained sediment samples are poorly sorted which might be related to the occurrence of pumices (Fig. 10A). These sediments also show better sorting with increasing mean grain diameter throughout the size range of 5 to 7 phi. Samples from tephra layers exhibit greater variability in sorting ranging from well-sorted to poorly-sorted. A further classification of the sieve analysis using Folk's (1954) textural groupings shows a majority of the sediments have silt (93 samples) or sandy silt (43 samples) composition (Fig. 10B). Other classes identified were silty sand (3 samples) and sand (11 samples).

The numbers of mean grain size, kurtosis, and skewness together with the other physical properties are given in supplementary Table S3. Overall, the background hemipelagic sediments have low skewness typically ranging between -0.1 and 0.1 meaning that the grain size distribution is mostly normal in the samples. On the other hand, the tephra layers have high skewness values ranging from 0.3 to 0.8 and have a larger abundance of coarse material with little clay (Table S3). Hence, they show a non-normal or non-gaussian distribution of the grain size.

4.3.4 Sediment physical properties

GRA bulk densities range from a minimum of 1.2 g/cm³ to a maximum of 2 g/cm³, with an average of 1.6 g/cm³ (Fig. 11). Most significant changes in GRA densities are associated with tephra layers which show lower values down to 1.2 g/cm³ (Fig. 11). The SKP-II tephra layer density shows a distinct bimodal shape (two peaks and a low) in the GRA density plots and is marked by a significant drop in density in all five cores (Fig. 11). This bimodal shape is correlated to observed changes in grain size distribution through the layer which probably relates to changes in the dynamics of the volcanic eruption and/or settling velocities of particles in the water column that ultimately affect porosity. The SKP-II layer density contrast between the cores could be related to the amount of clay that has percolated in the layer or, to some extent, spatial changes in the abundance of lithics. There are also other low-density layers associated with tephra layers in the lower parts of the cores (Fig. 11).

Magnetic susceptibility ranges from 0 to 100 SI but is typically between 3 and 20 SI (Fig. 11). The most striking feature of the MS records is a series of major increases or spikes in the cores that are associated with tephra layers (Fig. 11). These spikes are most prevalent in the tephra layers that contain lithic fragments whereas they are less pronounced in the tephra layers that do not include significant lithic fragments or magnetite. Hence, MS spikes in the study area are primary signals reflecting the presence of tephra layers that are rich in iron oxide minerals, especially magnetite. Uncommon peaks in background hemipelagic sediments might be related to the concentration of fine tephtras (e.g., glass shards) embedded in these deposits (Fig. 11).

Shear strength values gradually increase down the core ranging from 5 kPa near the seafloor to over 15 kPa at a subsurface depth of 4 m (Fig. 11). The MTD unit in core P08A also shows higher shear strengths compared to the background hemipelagic sediments.

Reflectance values of L^* represent luminosity or total reflected light, resulting from dark and light color alternations. Throughout all cores, L^* values fluctuate between 40 and 80 (Fig. 11). Significant changes in the L^* values occur only in association with the presence of darker (organic-rich) and lighter (carbonate-rich) sediments. No consistent relationship occurs between the changes in L^* and other physical properties.

There is also no correlation between the mean grain size and physical properties of the sediments such as the bulk density, shear strength, and magnetic susceptibility (Table S3).

4.4 Timing of submarine landslides and average sedimentation rate

Cyclic variations of dark and light layers in sediments from the East Sea reflect orbital and millennial-scale changes in palaeoceanographic conditions and have been widely used to establish high-resolution age models of sediments (e.g., Kido et al., 2007; Irino et al., 2018). We established an age model by correlating sediment lightness (L^*) variations in IODP drill core U1430 (see Fig. 1B for location) with those in core P11, which appears to have retrieved the longest record (ca. 140 kyr; Fig. 12A). The ages and their composite depths at Site U1430 were directly taken from the interpretation of Tada et al. (2018) (see their Table S1). The occurrence of tephra layers (i.e., SKP-I; ca. 40-41 ka old; SKP-II; ca. 60-61 ka old; Chun et al., 2007; Lim et al., 2013) confirms that the age correlation is valid. Depth-to-age conversion for the other sediment cores is based on correlations of L^* and tephra layers (Fig. 12A). In particular, the thick tephra layers (i.e., SKP-II) provide the best stratigraphic markers among our cores.

The age of the sediment that drapes landslide deposits provides a rough indication of the age of slope failure. The established age model indicates that the landslide deposits in core P08A imaged on the chirp seismic profile (Fig. 5D) occurred around or before ca. 84 ka (late Marine Isotope Stage (MIS)

5) (Fig. 12A-B).

Sedimentation rates on the upper slope are less than 8 cm/kyr since between ~150 and 12 ka and <2 cm/kyr during the Holocene (Fig. 12C). In contrast, sedimentation rates at IODP U1430 are two to three times higher (between ca. 6 to 8 cm/kyr) than that of our coring sites for the same time interval.

4.5 Relationship between glide (failure) planes and core lithology

The glide planes (failure planes) of the observed landslides were not sampled because they are buried out of the reach (> 8 m) of conventional piston coring. Hence, the acoustic reflectors associated with failure planes were traced into areas of undisturbed sediment and were correlated to depth within the existing deep drill cores from the nearby IODP Site U1430. In total, we trace nine distinct high-amplitude continuous shallow reflectors including the seabed throughout the area (Fig. 13A). Among them, magenta and red seismic horizons correspond to the failure planes of the submarine landslides. Overall, all of these high-amplitude continuous reflectors correspond well with thick pumice-rich intervals that are embedded within finer hemipelagic sediments (Fig. 13B).

The reflectors corresponding to failure horizons (magenta and red; Fig. 13A-B) apparently correlate to thicker tephra intervals in the cores. For example, the magenta reflector corresponds to a 16 cm thick tephra layer in IODP U1430 Holes B and C (Fig. 13C-D) and the red reflector corresponds to a 9 cm thick tephra interval in Holes B and C (Fig. 13E-F). These tephra layers are bracketed by clay-rich hemipelagic sediments.

5. Discussion

An integration of MBES, seismic reflection, and piston core data reveals abundant evidence of MTDs in the southern margin of the ESKP (Figs. 2, 6, and 7). MBES data demonstrates that mass wasting processes (including debris flows, slides/slumps) are associated with at least 50 landslides, that have affected a total area of ~470 km². This surface comprises 20% of the studied seafloor (Fig. 2), making the concentration of landslides along the ESKP margin one of the highest in the world (see below).

The characterization of landslides in this study complements previous results from submarine landslides around the margins of the Ulleung Basin (Fig. 1), in particular the work of Horozal et al. (2019) that analyzed and mapped at least 38 submarine landslides with areas and volumes ranging between 20 to 800 km² and 0.1 to 340 km³, respectively. Some notable differences exist between submarine landslides and associated sediments in the southern ESKP margin and the Ulleung Basin margins, which suggests different or variable dynamics of landslide formation. First, the ESKP lacks giant submarine landslides in comparison to those observed on the southern margin of the UB (ca. up to 340 km³). Some studies (i.e., Moscardelli and Wood, 2016) suggest that the volume of slope failures

may largely be related to the presence of large fluvial systems and high sediment accumulation in shelf and upper slope environments. The southern margin of the UB is fed by large river systems that may have contributed to the voluminous slope failures (Horozal et al., 2019). In contrast, drainage patterns indicate the supply of terrigenous sediment to the ESKP margin was more limited (Tada et al., 2015; this study). Second, contrary to previous observations reported from the UB margin sediments (e.g., Cukur et al., 2016; 2020), we observed volcanic fragments (volcanic glass shards, minerals, and lithics) in almost all the sampled fine-grained hemipelagic sediments. This unambiguously indicates that there has been a regular supply of tephras to the ESKP margin during the latest Quaternary. This is consistent with the proximity of the study area to the Ulleungdo volcano which has been active throughout the Quaternary (Chen et al., 2018, and references therein). Third, the water depths of scarps in the UB margins lie at shallower depths (between 150 m to 1130 m) than the scarps in our study area. Finally, the age of landslides in the UB margins is relatively younger (between ca. 11 ka to 20 ka; Fig. 12B) than that of landslides identified in our study area.

As already noted above, the concentration of landslides in the ESKP study area is one of the highest in the world. The cumulative failed slope area in the ESKP (20% of the studied seafloor) is higher than at landslide-prone margins, including the middle Atlantic (16%; Twichell, et al., 2009), the Great Barrier Reef margin (12.6 %; Bernab  u et al., 2022), the New Jersey margin (9.5%; McAdoo et al., 2000), and the eastern U.S. Pacific margin (3%; McAdoo et al., 2000). The spatial density of landslides in the ESKP is close to observations in the Mediterranean Sea (18%; Urgeles and Camerlenghi, 2013) and the eastern Mediterranean Israeli continental slope (20%; Katz et al., 2015). High supply of terrigenous sediments and active tectonics are interpreted as the two main reasons for the high concentration of landslides in these areas. In contrast, the margin of ESKP has low sediment supply and is a volcanically influenced geological setting that is likely influenced by other mechanisms of landslide formation.

5.1 Landslide failure styles

The blocky versus disintegrative failure style of submarine landslides is commonly used to assess risks for tsunami generation (Riedel et al., 2018; Lenz and Sawyer 2021). Thicker blocky landslides, for instance, are more likely to produce a tsunami compared to disintegrative slides (McAdoo and Watts 2004; Watts 2004; Tappin et al., 2002; Lenz and Sawyer, 2021). The character of the landslides largely depends on the depth of the basal glide plane, the strength of the sediment, earthquake shaking patterns, fluid flow, and regional slope gradient (McAdoo et al., 2000; Sultan et al., 2004; Moernaut and De Batist, 2011; Piper et al., 2012; Sawyer et al., 2012). MBES data and the relationship between landslide parameters in the upper, middle, lower, and lowermost slopes of the ESKP margin (Figs. 3 and 5) indicate that there are some key differences in landslide character between the lower and upper slopes.

There is a continuum between the headwall height and slope from upper to lower slope except for a few outliers characterized by high headwall heights (Fig. 5B). Some of these outliers are the same outlier shown in figure 5A (e.g., SL9, and SL13) and are correlated to faults (Fig. S3). Therefore, there are two groups of landslides distinguishable based on their headwall scarp location. The first group consists of landslides with taller scarps and requires a distinct mechanism of slope failure that could be related to the occurrence of faults. The second group consists of landslides with no relation to fault scarps and smaller headwall scarps. A continuum is observed between the length of slope failure and slope angle of these slides, which is correlated to the water depth and overall morphology of the seafloor along the south of the ESKP (Fig. 5).

Landslides are commonly more blocky and have not moved far when the slope increases towards the lowermost part of the ESKP margin (Fig. 3D). The blocky character of these landslides suggests they occurred relatively long after the deposition of the sediments, allowing partial consolidation through early diagenesis. As a result, these sediments would be more cohesive and would not disaggregate easily, thus forming local slump/slide blocks rather than far travelling MTDs. Stronger or consolidated sediments tend to remain intact during a slope failure and produce a blocky failure as in the case of the Oregon continental margin (McAdoo and Watts, 2004; Lenz and Sawyer, 2021), offshore Papua New Guinea (Tappin et al., 2002), offshore Southern California (Watts, 2004), and Cascadia subduction zone (Hill et al., 2022). Similarly, disaggregated blocky landslides on the Canadian continental margin occur on the steep upper slope where sediments are consolidated by depths of 50 m or more (Piper et al., 2012). According to the study of McAdoo et al. (2000) on the southern Oregon margin, the failures' headscarp morphology can be used to infer sediment strength, with steep headscarps occurring in a stronger material. This is in line with our observations in the lower slope of the ESKP. The flat sea floor at the very base of the ESKP margin may have also assisted in limiting runout distances and associated disaggregation during transport.

Landslides on the upper- to middle-ESKP margin where slope gradients are lower appear more disintegrative and are associated with smoother evacuated areas (Figs. 3A-B). Morphological and core observations in the shallower areas indicate that less consolidated (weaker) sediments have been mobilized into debris flows. This observation is consistent with observations of McAdoo et al. (1997) from the Cascadia convergent margin, who noted that lower headwall scarp heights along with the smooth appearance of the upper slope are associated with weaker sediments susceptible of post-failure lose of cohesion. Slope gradient is clearly not the sole possible control of the style and character of the landslides - this also must depend on sediment characteristics and the amount and frequency of earthquake-generated ground motions (Moernaut and De Batist, 2011; Piper et al., 2012). Other processes that can increase the runout distances of failed sediments are hydroplaning over a smooth surface (Mohrig et al., 1998) or the presence of basal layers with low friction characteristics (e.g.,

Hinlopen or Sahara Slide; Vanneste et al., 2006; Georgiopoulou et al., 2010). We rule out the latter process because fresh tephra, which correlate to basal glide planes of the observed landslides in our study area, may have high frictional resistance compared to common sands or sand-clay mixtures (Wiemer and Kopf, 2015).

The slope failures that occur on the lowermost slope may suggest that the southern margin of the ESKP may be at higher risk of generating tsunamis due to the blocky and cohesive mode of slope failures. However, landslide-generated tsunamis are also largely dependent on other parameters such as slide thickness, maximum velocity, initial acceleration, and water depth (Watts, 2004; Harbitz et al., 2006). Considering their small size (<1 km³) and deeper water depths (>2000 m), the submarine landslides observed in the study area may not be tsunamigenic. Full assessment of their tsunami potential would however require comprehensive tsunami modeling.

5.2 Do tephra layers control submarine landslides on the ESKP?

Previous work suggests that altered (clay-rich) ash beds can represent mechanically weak layers and form glide planes in slope sediment sequences (Locat et al., 2014; Wiemer and Kopf, 2015; Kluger et al., 2017; Miramontes et al., 2018; Sammartini et al., 2019). Our ESKP work suggests a correlation between the thick layers of coarse tephra and some of the glide planes (Fig. 13), however the mineralogy and geochemistry of the studied tephra layers at the depth of the glide planes show that they are fresh and do not contain abundant clay minerals. These layers are instead composed of poorly sorted and cohesive granular materials, with likely a higher porosity than the rest of the hemipelagic sediments. Hence another explanation to explain the correlation of the tephra layers to glide planes could be their distinctive hydraulic properties and controls of fluid pressure within the sedimentary sequence.

Water escape structures occur broadly along the margin (Fig. 6A-B) and there is evidence of fluid flows in IODP cores from this area (Tada et al., 2015), thus showing that pore pressure is high enough in the sediments to create upward percolation of water (Kluger et al., 2023). In this context, fluid overpressure can be concentrated in porous layers such as those formed by coarse tephra deposits. We suggest that tephra layers acted as landslide planes because they were simply less resistant to earthquake-induced liquefaction than bracketing cohesive sediment, which also may have acted as permeability barriers preventing dissipation of pore water pressure. During an earthquake, the effective stress in these tephra layers would have been reduced by the excess pore water pressure until the material liquefied at zero effective stress. Then, the tephra layer lost its strength and stiffness and a failure surface formed, resulting in landsliding. This hypothesis is also supported by higher pore fluid pressures in coarse tephra layers drilled during IODP Expedition 340 at, e.g., sites U1397, U1398, and U1399, offshore Martinique (Lafuerza et al. 2014). It is also worth noting that undrained ring shear tests on volcanic sands taken at a depth of 188-189 m below the sea floor from the Nankai Trough generated

a high pore water pressure during cyclic loading (Sassa et al., 2012).

Two main mechanisms have previously been proposed for slide nucleation controlled by fluid behavior in tephra layers: (i) increased pore pressure due to high hydraulic conductivity, and (ii) increase in pore pressure/liquefaction due to rearrangement of asymmetrical particles (Sammartini et al., 2019). Although the rearrangement of asymmetrical particles is unlikely in the studied tephra due to the occurrence of subrounded to rounded pumices, particle reorganization by earthquake-generated shaking can lead to granular convection and compaction (Fig. 14). This mechanism has been observed in experiments on sediment liquefaction (Ribi re et al., 2005) and supports a new hypothesis for the creation of free water within, and fluidization of, tephra layers.

5.3 Controls on the timing of landslide nucleation

Different external geological controls can influence the recurrence of submarine landslides and their temporality in the study area. Conceptually, a landslide or a cluster of landslides occur when nucleation conditions are met, which can be explained by (i) internal mechanical “maturation” of the sediments, e.g., pore pressure buildup, and (ii) external geological controls that can modulate the rate and possibly the nature of changes in the mechanical behavior of the sediments, e.g., the rate of sedimentation or earthquakes affecting burial compaction and/or dewatering of the sediment (Fig. 15). The frequency and nature of the landslides will depend on the mechanisms at play. Reciprocally, the timing of landslide formation can offer a valuable insight into the controls of landslide nucleation in a given geological environment. Available age constraints from landslides along the margin of the ESKP suggest that they predominantly occurred ca. 84 ka ago, with apparently more limited or no activity in younger times. As already discussed above, this contrasts with the younger (ca. 11-20 ka) ages of landslide formation from the Ulleung Basin margins (Lee et al., 2010; Cukur et al., 2020), suggesting that the study area experienced a specific phase of increased landslide formation.

Geological controls on landslide formation generally include the presence of methane in subsurface sediments, which can increase the pore fluid pressure and thereby decrease the effective stress of seafloor sediment and ultimately lead to failure (e.g., Field, 1990; B niz et al., 2003; Sultan et al., 2004; Kaminski et al., 2020). However, the influence of methane on the formation of ESKP margin landslides can be ruled out in the study area because only low TOC and methane concentrations were measured in the sediments from nearby IODP holes (Tada et al., 2015; see their Fig. 36). Rapid sedimentation (i.e., > 100 cm/kyr) can also cause elevated pore fluid pressure in the sub-seafloor strata and trigger slope failures (Dugan and Flemings, 2000; Hill et al., 2017). However, the sedimentation rates in the study area are relatively low (< 8 cm/kyr; Fig. 12C) and there is no change in the sedimentation rate at the time of landslide occurrence, making therefore this hypothesis unlikely.

Earthquakes are another processes that can influence landslide formation, as cyclic loading and

increased fluid pressure cause failures due to sediment weakening (Hampton et al., 1996; Locat and Lee, 2002; Masson et al., 2006). Landsliding may have been triggered by strong ground motions around the ESKP margin associated with rupture of nearby faults (see Figs. 2 and S3) or volcanic activity. The faulting and folding, which are evident in the MBES data and chirp seismic profiles (Figs. 6A, 6D, and 7D) was most likely accompanied by large-magnitude earthquakes. Empirical relationships between fault length and earthquake magnitude (Wells and Coppersmith, 1994) suggest that the >40-km-long fault near our study area (see Fig. S3B) could generate an earthquake with a moment magnitude (M_w), of 7.0 or higher. The maximum distance at which liquefaction may occur is mainly a function of moment magnitude (Maurer et al. 2015). For instance, an earthquake with a magnitude of 7 may trigger liquefaction over large distances of up to 80 km (Maurer et al., 2015). The observed landslides in our study area occurred between 2 km to 40 km away from the major faults (i.e., a 40 km-long fault) hence these faults could have easily caused liquefaction in our study area.

The potential for liquefaction decreases with increasing overburden pressure, such that the maximum reported depth of liquefaction effects is 10 m (Owen and Moretti, 2011). The youngest glide plane associated with the tephra layer is buried by < 6 m of hemipelagic sediments, therefore, the liquefaction susceptibility of these tephra layers is likely to have persisted since their deposition. Also, liquefaction susceptibility commonly decreases with time after deposition due to post-depositional processes such as cementation (Kluger et al., 2023). However, the tephra layers in our study area are fresh and have not undergone cementation, precluding a decrease in liquefaction susceptibility due to cementation. Once loaded by an earthquake, the tephra layers may have experienced granular convection and “liquefaction”, with free water concentrating at the top of these layers to trigger a landslide (Fig. 16). This may have been aided by the presence of impermeable organic-rich muddy layers, which may have prevented seepage and led to an increase in pore pressure at the tephra-sediment interface, as noted by Kluger et al. (2023) in organic lake sediments above and below the tephra from the Hamilton lowlands, New Zealand. Unfortunately, limited age controls do not allow us to determine whether sedimentation rate or seismicity might have controlled the timing of recurrence and possible cyclicity of landslides in the study area. Additional coring is required to date the landslides and determine patterns in their temporal and spatial recurrence. This is important for the state of knowledge in which one can start predictions, develop hazard maps, and understand landslide dynamics.

6. Conclusions

By combining MBES, high-resolution chirp seismic reflection, and sediment piston core data we document the morphology of submarine landslides from the southern margin of the ESKP and infer their preconditioning and triggering factors. At least 50 translational landslides were identified at water depths of 980 to 2300 m. The cumulative surface of failed slope is 20% of the studied seafloor, indicating that mass wasting is a significant process shaping the southern ESKP margin. Slope failures

on the gentle (2.2°) upper slope to middle slope are mostly disintegrative with longer runouts, whereas those on the steeper lower slope ($\sim 6^\circ$) are blocky landslides with shorter runouts. Core observations indicate that landslide deposits consist of debris flows and slides/slumps interbedded with hemipelagic mud and coarse-grained tephra. Thick coarse tephra layers seen in the cores correlate with some of the glide planes. These tephras are coarse, poorly sorted, and relatively fresh (not altered) and thus cannot be considered as clay-rich weak layers. However, a higher abundance of thick porous tephra layers could have helped promote fluid flow, with nucleation of landslides triggered by earthquake-induced overpressure. Upon loading by an earthquake, the poorly sorted tephra layers may have undergone granular convection leading to (i) compaction and release of pore fluid and (ii) rapid accumulation of the fluid at the interface between the tephra and the overlying organic-rich muddy hemipelagic sediments. Pore pressure build-up under the hemipelagic cap may have fostered liquefaction of some of the sediment, thereby triggering landslides. An overpressure build-up along the tephra layers may have preconditioned the slope to fail while large earthquakes may have triggered the landslides. These mechanisms could prove significant to understand the formation of landslides in margins close to shallow marine to subaerial volcanoes, where explosive volcanism leads to the deposition of tephra layers within hemipelagic deposits.

Data availability

The data used in this paper are classified but can be shared through cooperative projects after 3 years of the moratorium period. Interested readers should make a request to the corresponding author (D.C.).

Declaration of Competing Interest

The authors in this paper declare no conflicts of interests.

Acknowledgements

This study was supported by the project entitled “Geological survey in the Korean Peninsula and publication of the geological maps (GP2020-009)” of the Korea Institute of Geoscience and Mineral Resources (KIGAM) funded by the Industry and Energy and the Ministry of Science. We would like to thank Editor Dr. Michele Rebesco, Dr. Samuel Y. Johnson, and two anonymous reviewers for their constructive comments. We thank the captains, officers, crew and scientific parties of the *RV Tamhae II* for help in data collection.

Supplementary table captions

Table S1: Core locations, water depths (m), and core lengths (cm).

Table S2: Distribution of landslides and their geomorphic parameters

Table S3: Mean grain size, sorting, skewness, and kurtosis as well as the physical properties of samples from the tephra layers and background hemipelagic sediments.

References

- Arai, F., Oba, T., Kitazato, H., Horibe, Y., Machida, H., 1981. Late Quaternary tephrochronology and paleo-oceanography of the sediments of the Japan Sea. *The Quaternary Research (Daiyonki-Kenkyu)* 20, 209–230. <https://doi.org/10.4116/jaqua.20.209>
- Asadi, M.S., Asadi, M.B., Orense, R.P., Pender, M.J., 2018. Undrained cyclic behavior of reconstituted natural pumiceous sands. *Journal of Geotechnical and Geoenvironmental Engineering* 144(8), 04018045. [https://doi.org/10.1061/\(ASCE\)GT.1943-5606.0001912](https://doi.org/10.1061/(ASCE)GT.1943-5606.0001912)
- Bahk, J.J., Chough, S.K., Han, S.J., 2000. Origins and paleoceanographic significance of laminated muds from the Ulleung Basin, East Sea (Sea of Japan). *Mar. Geol.* 162, 459–477.
- Bernabéu, A.G., Cabrera, J.L., Webster, J.M., Beaman, R.J., 2022. Submarine landslide morphometrics and slope failure dynamics along a mixed carbonate-siliciclastic margin, north-eastern Australia. *Geomorphology* 403,108179.
- Bünz, S., Mienert, J., Berndt, C., 2003. Geological controls on the Storegga gas-hydrate system of the mid-Norwegian continental margin. *Earth and Planetary Science Letters* 209(3–4), 291–307. [https://doi.org/10.1016/S0012-821X\(03\)00097-9](https://doi.org/10.1016/S0012-821X(03)00097-9).
- Camerlenghi, A., Urgeles, R., Fantoni, L. (2010). A Database on Submarine Landslides of the Mediterranean Sea. In: , *et al.* *Submarine Mass Movements and Their Consequences. Advances in Natural and Technological Hazards Research*, vol 28. Springer, Dordrecht.
- Chaneva, J., Kluger, M.O., Moon, V.G., Lowe, D.J., Orense, R.P. 2023. Monotonic and cyclic undrained behaviour and liquefaction resistance of pumiceous, non-plastic sandy silt. *Soil Dynamics and Earthquake Engineering* 168, 107825
- Chaytor, J.D., Uri, S., Solow, A.R., Andrews, B.D., 2009. Size distribution of submarine landslides along the US Atlantic margin. *Marine Geology* 264,16–27
- Chen, S.S., Lee, S.G., Lee, T.J., Lee, Y.S., Liu, J.Q., 2018. Multi-stage magmatic plumbing system of the volcano: A case study from Ulleung Island, South Korea. *Lithos* 314–315, 201–215. <https://doi.org/10.1016/j.lithos.2018.05.028>
- Choi, H.-O., Kim, J., Oh, J., Kim, C.H., Choi, S.Y., Kim, W.H., Park, C.H., 2022. Petrogenesis of submarine volcanic rocks dredged from Dokdo, Ulleungdo, and the neighboring seamounts in the East Sea: Constraints from mineral chemistry, geochemistry, and $^{40}\text{Ar}/^{39}\text{Ar}$ ages. *Lithos* 426–427, 106783. <https://doi.org/10.1016/j.lithos.2022.106783>
- Chun, J.-H., Han, S.-J., Cheong, D.-K., 1997. Tephrostratigraphy in the Ulleung Basin, East Sea: Late Pleistocene to Holocene. *Geosciences Journal* 1, 154–166. <https://doi.org/10.1007/BF02910207>
- Chun, J.-H., Cheong, D., Ikehara, K., Han, S.-J., 2007. Age of the SKP-I and SKP-II tephras from the southern East Sea/Japan Sea: Implications for interstadial events recorded in sediment from marine isotope stages 3 and 4. *Palaeogeography, Palaeoclimatology, Palaeoecology* 247, 100–114. <https://doi.org/10.1016/j.palaeo.2006.11.024>

- Chun, J.-H., Cheong, D., 2020. Origin of compositional diversity of marine tephra during the late Middle Pleistocene B-KY1 Baekdusan volcanic eruption. *Applied sciences* 10, 4469. doi:10.3390/app10134469.
- Cukur, D., Kim, S.-P., Kong, G.-S., Kim, J.-K., Bahk, J.-J., Horozal, S., Um, I.-K., Lee, G.-S., Chang, T.-S., Ha, H.-J., Volker, D., Kim, J.-K., 2016. Geophysical evidence and inferred triggering factors of submarine landslides on the western continental margin of the Ulleung Basin. *East Sea. Geo. Mar. Lett.* 36 (6), 425–444.
- Cukur, D., Um, I.-K., Chun, J.-H., Lee, G.-S., Kim, S.-R., Bahk, J.-J., Urgeles, R., Horozal, S., 2020. Factors leading to slope failure on a sediment-starved margin: The southwestern continental margin of the East Sea, Korea. *Mar. Geol.* 428 (106282), 1–21. <https://doi.org/10.1016/j.margeo.2020.106282>.
- Damuth, J.E., Olson, H.C., 2015. Latest Quaternary sedimentation in the northern Gulf of Mexico Intraslope Basin Province: I. Sediment facies and depositional processes. *Geosphere* 11 (6), 1689–1718. doi: <https://doi.org/10.1130/GES01090.1>
- de Cristofaro, M., Olivares, L., Orense, R., Asadi, M., Netti, N., 2022. Liquefaction of volcanic soils: undrained behavior under monotonic and cyclic loading. *Journal of Geotechnical and Geoenvironmental Engineering* 148(1), 04021176.
- Dugan, B., Sheahan, T.C., 2000. Overpressure and Fluid Flow in the New Jersey Continental Slope: Implications for Slope Failure and Cold Seeps. *Science* 289(5477), 288–291.
- Field, M.E., 1990. Submarine landslides associated with shallow seafloor gas and gas hydrates off northern California. United States: N. p., 1990. Web.
- Gatter, R., Clare, M.A., Kuhlmann, J., Huhn, K., 2021. Characterisation of weak layers, physical controls on their global distribution and their role in submarine landslide formation. *Earth Science Reviews* 223, 103845.
- Georgiopoulou, A., Masson, D.G., Wynn, R.B., Krastel, S., 2010. Sahara Slide: Age, initiation, and processes of a giant submarine slide. *Geochem. Geophys. Geosyst.*, 11, Q07014.
- Hampton, M.A., Lee, H.J., Locat, J., 1996. Submarine landslides. *Reviews of Geophysics* 34 (1), 33–59.
- Harbitz, C.B., Løvholt, F., Pedersen, G., Masson, D.G., 2006. Mechanisms of tsunami generation by submarine landslides: A short review. *Norw. J. Geol.*, 86(3), 255–264
- Harders, R., Kutterolf, S., Hensen, C., Moerz, T., Bruekmann, W., 2010. Tephra layers: A controlling factor on submarine translational sliding?. *Geochem. Geophys. Geosyst.*, 11, Q05S23.
- Hill, J.C., Brothers, D.S., Craig, B.K., ten Brink, U.S., Chaytor, J.D., Flores, C.H., 2017. Geologic controls on submarine slope failure along the central U.S. Atlantic margin: insights from the Currituck Slide complex *Mar. Geol.*, 385 (2017), pp. 114-130
- Hill, J.C., Watt, J.T., Brothers, D.S., 2022. Mass wasting along the Cascadia subduction zone: Implications for abyssal turbidite sources and the earthquake record. *Earth and Planetary Science Letters* 597,117797. <https://doi.org/10.1016/j.epsl.2022.117797>.
- Horozal, S., Bahk, J.-J., Lee, S.H., Cukur, D., Urgeles, R., Kim, G.Y., Kim, S.-P., Ryu, B.-J., Kim, J.-H., 2019. Mass-wasting processes along the margins of the Ulleung Basin, East Sea: insights from multichannel seismic reflection and multibeam echosounder data. In: Lintern, D.G., Mosher, D.C., Moscardelli, L.C., et al. (Eds.), *Subaqueous Mass Movements and their Consequences: Advances in Process Understanding, Monitoring and Hazard Assessments*, 477. Geological Society, London, Special Publications, pp. 107–120. <https://doi.org/10.1144/SP477.18>.

- Horozal, S., Kim, G.Y., Cukur, D., Bahk, J.J., Buchs, D., Ryu, B.R., Lee, G.H., Kim, S.P., 2017. Sedimentary and structural evolution of the Eastern South Korea Plateau (ESKP), East Sea (Japan Sea). *Marine and Petroleum Geology*, 85, 70–88
- Hyodo, M., Hyde, A., Aramaki, N., 1998. Liquefaction of crushable soils. *Geotechnique*, 48(4), 527–543
- Ikehara, K., 2015. Marine tephra in the Japan Sea sediments as a tool for paleoceanography and paleoclimatology. *Progress in Earth and Planetary Science* 2, 36. <https://doi.org/10.1186/s40645-015-0068-z>
- Irino, T., Tada, R., Ikehara, K., Sagawa, T., Karasuda, A., Kurokawa, S., Seki, A., Lu, S., 2018. Construction of perfectly continuous records of physical properties for dark-light sediment sequences collected from the Japan Sea during Integrated Ocean Drilling Program Expedition 346 and their potential utilities as paleoceanographic studies. *Prog Earth Planet Sci* 5, 23 (2018). <https://doi.org/10.1186/s40645-018-0176-7>
- Kaminski, P., Sager, T., Grabe, J., Urlaub, M., 2021. A new methodology to assess the potential of conjectural trigger mechanisms of submarine landslides exemplified by marine gas occurrence on the Balearic Promontory. *Engineering Geology* 295, 106446. <https://doi.org/10.1016/j.enggeo.2021.106446>.
- Kang, M.H., Han, H.C., Yun, H., Kong, G.S., Kim, K.O., Lee, Y.S., 2007. 3D gravity modelling for Anyongbok Seamount in the East Sea. *Mar. Geophys. Res.* 28, 257–269. <https://doi.org/10.1007/s11001-007-9030-9>
- Katz, O., Reuven, E., Aharonov, E., 2015. Submarine landslides and fault scarps along the eastern Mediterranean Israeli continental-slope. *Marine Geology* 369, 100–115.
- Kluger, M.O., Ilanko, T., Lowe, D.J., Moon, V.G., Chaneva, J., et al. 2023. Tephra seismites preserved in unconsolidated organic lake sediments in the Hamilton lowlands, New Zealand, indicate paleoearthquake activity since 17.6 ka. In: *Book of Abstracts, IAVCEI Scientific Assembly, 30 Jan-3 Feb 2023, Rotorua, New Zealand*. p: 503. <https://doi.org/10.13140/RG.2.2.29974.42568>
- Kluger, M.O., Moon, V.G., Kreiter, S., Lowe, D.J., Churchman, G.J., Hepp, D.A., Seibel, D., Jorat, M.E., Morz, T., 2017. A new attraction-detachment model for explaining flow sliding in clay-rich tephra. *Geology* 45(2), 131–134. <https://www.doi.org/10.1130/G38560.1>
- Kido, Y., Minami, I., Tada, R., Fujine, K., Irino, T., Ikehara, K., Chun, J.H., 2007. Orbital-scale stratigraphy and high-resolution analysis of biogenic components and deepwater oxygenation conditions in the Japan Sea during the last 640 kyrs using XRF microscanner. *Palaeogeogr. Palaeoclimatol. Palaeoecol.* 247, 32–49
- Kim, C.H., Park, J.W., Lee, M.Y., Park, C.H., 2013. Detailed Bathymetry and Submarine Terraces in the Coastal Area of the Dokdo Volcano in the Ulleung Basin, the East Sea (Sea of Japan). *Journal of Coastal Research* 65, 523–528. <https://doi.org/10.2112/SI65-089.1>
- Kim, H.J., Lee, G.H., Choi, D.L., Jou, H.T., Li, Z., Zheng, Y., Kim, G.Y., Lee, S.H., Kwon, Y.K., 2015. Back-arc rifting in the Korea Plateau in the East Sea (Japan Sea) and the separation of the southwestern Japan Arc from the Korean margin. *Tectonophysics*, 638, 147–157.
- Kuhlmann, J., Asioli, A., Trincardi, F., Klügel, A., Huhn, K., 2017. Landslide frequency and failure mechanisms at NE Gela Basin (Strait of Sicily). *J. Geophys. Res. Earth Surf.* 122, 2223–2243.
- Laberg, J.S., Kawamura, K., Amundsen, H., Baeten, N., Forwick, M., Rydningen, T.A., Vorren, T.O., 2014. A submarine landslide complex affecting the Jan Mayen Ridge, Norwegian–Greenland Sea:

- slide- scar morphology and processes of sediment evacuation. *Geo-Marine Letters* 34, 51–58.
- Lafuerza, S., Le Friant, A., Manga, M., Boudon, G., Villemant, B., Stroncik, N., et al. 2014. “Geomechanical Characterizations of Submarine Volcano Flank Sediments, Martinique, Lesser Antilles Arc, Chap. 7,” *Submarine Mass Movements and Consequences, Advances in Natural and Technological Hazards Research*. S. Krastel, J.-H. Behrmann, D. Völker, M. Stipp, C. Berndt, R. Urgeleset al. Editors (Cham, Switzerland: Springer International), 73.
- Lee, G. H., Yoon, Y., Nam, B. H., Lim, H., Kim, Y.-S., Kim, H. J., Lee, K., 2011. Structural Evolution of the Southwestern Margin of the Ulleung Basin, East Sea (Japan Sea) and Tectonic Implications. *Tectonophysics* 502 (3), 293–307
- Lee, S.H., Bahk, J.J., Kim, H.J., Lee, K.E., Jou, H.T., Suk, B.C., 2010. Changes in the frequency, scale, and failing areas of latest Quaternary (< 29.4 cal. ka B.P.) slope failures along the SW Ulleung Basin, East Sea (Japan Sea), inferred from depositional characters of densely dated turbidite successions. *Geo-Marine Letters* 30, 133–142.
- L’Heureux, J.S., Longva, O., Steiner, A., Hansen, L., Vardy, M.E., Vanneste, M., Haflidason, H., Brendryen, J., Kvalstad, T.J., Forsberg, C.F., Chand, S., Kopf, A., 2012. Identification of Weak Layers and Their Role for the Stability of Slopes at Finneidfjord, Northern Norway. In: , *et al. Submarine Mass Movements and Their Consequences. Advances in Natural and Technological Hazards Research*, vol 31. Springer, Dordrecht.
- Lenz, B.L., Sawyer, E.D., 2021. Mass transport deposits in reflection seismic data offshore Oregon, USA. *Basin Res.* 34 (1), 81–98.
- Lim, C., Toyoda, K., Ikehara, K., Peate, D.W., 2013. Late Quaternary tephrostratigraphy of Baegdusan and Ulleung Volcanoes using marine sediments in the Japan Sea/East Sea. *Quaternary Research* 80, 76–87. <https://doi.org/10.1016/j.yqres.2013.04.002>
- Locat, J., Lee, H.J., 2002. Submarine landslides: advances and challenges. *Can. Geotech. J.*, 39, 193–212.
- Locat, J., Leroueil, S., Locat, A., Lee, H., 2014. Weak Layers: Their Definition and Classification from a Geotechnical Perspective. In: , *et al. Submarine Mass Movements and Their Consequences. Advances in Natural and Technological Hazards Research*, vol 37. Springer, Cham.
- Lowe, D.J., 2011. Tephrochronology and its application: a review. *Quaternary Geochronology* 6(2), 107-153. <https://doi.org/10.1016/j.quageo.2010.08.003>
- Machida, H., Arai, F., 1983. Extensive ash falls in and around the sea of Japan from large late quaternary eruptions. *Journal of Volcanology and Geothermal Research* 18, 151–164. [https://doi.org/10.1016/0377-0273\(83\)90007-0](https://doi.org/10.1016/0377-0273(83)90007-0)
- Machida, H., Arai, F., 1988. A review of Late Quaternary deep-sea tephtras around Japan. *Quat. Res. (Daiyonki-kenkyu)* 26, 227–242 (in Japanese, with English Abstr.).
- Masson, D.G., Harbitz, C.B., Wynn, R.B., Pedersen, G., Løvholt, F., 2006. Submarine landslides: processes, triggers and hazard prediction. *Phil. Trans. R. Soc. A.* 364, 2009–2039.
- Maurer, B.W., Green, R.A., Quigley, M.C., Bastin, S., 2015. Development of magnitude-bound relations for paleoliquefaction analyses: New Zealand case study. *Engineering Geology* 197, 253-266. <https://doi.org/10.1016/j.enggeo.2015.08.023>
- McAdoo, B.G., Orange, D.L., Screaton, E., Lee, H., Kayen, R., 1997. Slope basins, headless canyons, and submarine palaeoseismology of the Cascadia accretionary complex. *Basin Research* 9, 313–324.
- McAdoo, B.G., Pratson, L.F., Orange, D.L., 2000. Submarine landslide geomorphology, US

- continental slope. *Marine Geology* 169 (1–2), 103–136.
- McAdoo, B.G., Watts, P., 2004. Tsunami hazard from sub-marine landslides on the Oregon continental slope. *Marine Geology* 203(3–4), 235–245.
- McHugh, C.M.G., Damuth, J.E., Gartner, S., Katz, M.E., Mountain, G.S., 1996. Oligocene to Holocene mass-transport deposits of the New Jersey continental margin and their correlation to sequence boundaries. In: Mountain, G.S., Miller, K.G., Blum, P., Poag, C.W., Twichell, D.C. (Eds.), *Proceedings of the Ocean Drilling Program, Scientific Results*, vol. 150. pp. 189–228. <https://doi.org/10.2973/odp.proc.sr.150.016.1996>.
- McLean, D., Albert, P.G., Suzuki, T., Nakagawa, T., Kimura, J.I., Chang, Q., MacLeod, A., Blockley, S., Staff, R.A., Yamada, K., Kitaba, I., Haraguchi, T., Kitagawa, J., Smith, V.C., 2020. Refining the eruptive history of Ulleungdo and Changbaishan volcanoes (East Asia) over the last 86 kyrs using distal sedimentary records. *Journal of Volcanology and Geothermal Research* 389, 106669. <https://doi.org/10.1016/j.jvolgeores.2019.106669>.
- Miramontes, E., Sultan, N., Garziglia, S., Jouet, G., Pelleter, E., Cattaneo, A., 2018. Altered volcanic deposits as basal failure surfaces of submarine landslides. *Geology* 46 (7), 663–666. <https://doi.org/10.1130/G40268.1>.
- Moernaut, J., De Batist, M., 2011. Frontal emplacement and mobility of sublacustrine landslides: Results from morphometric and seismostratigraphic analysis. *Marine Geology* 285 (1–4), 29–45. <https://doi.org/10.1016/j.margeo.2011.05.001>.
- Mohrig, D., Ellis, C., Parker, G., Whipple, K.X., Hondzo, M., 1998. Hydroplaning of subaqueous debris flows. *GSA Bulletin* 110 (3), 387–394.
- Moscardelli, Lorena., Wood, Lesli., 2016. Morphometry of mass-transport deposits as a predictive tool. *GSA Bulletin* 128 (1-2), 47–80. doi: <https://doi.org/10.1130/B31221.1>
- Orense, R.P., Pender, M.J., Tai, A., 2014. Undrained cyclic shear strength of crushable sands. *International Journal of Geotechnical Engineering* 8(4), 426–430
- Orense, R., Pender, M., 2015. From micro to macro: An investigation of the geomechanical behaviour of pumice sand. *Volcanic Rocks and Soils* 45
- Owen, G., Moretti, M., 2011. Identifying triggers for liquefaction-induced soft-sediment deformation in sands. *Sedimentary Geology* 235(3-4), 141–147. <https://doi.org/10.1016/j.sedgeo.2010.10.003>
- Park, M.-H., Kim, I.-S., Shin, J.-B., 2003. Characteristics of the late Quaternary tephra layers in the East/Japan Sea and their new occurrences in western Ulleung Basin sediments. *Marine Geology* 202, 135–142. [https://doi.org/10.1016/S0025-3227\(03\)00287-1](https://doi.org/10.1016/S0025-3227(03)00287-1)
- Park, M.-H., Kim, J.-H., Kil, Y.-W., 2007. Identification of the late Quaternary tephra layers in the Ulleung Basin of the East Sea using geochemical and statistical methods. *Marine Geology* 244, 196–208. <https://doi.org/10.1016/j.margeo.2007.06.006>
- Piper, D., Mosher, D., & Campbell, D. (2012). Controls on the distribution of major types of submarine landslides. In J. Clague & D. Stead (Eds.), *Landslides: Types, Mechanisms and Modeling* (pp. 95–107). Cambridge: Cambridge University Press.
- Rivière, P., Richard, P., Delannay, R., Bideau, D., 2005. Importance of convection in the compaction mechanisms of anisotropic granular media. *Phys Rev E Stat Nonlin Soft Matter Phys.* 71(1 Pt 1):011304.
- Riedel, M., Cote, M.M., Urlaub, M., Geersen, J., Scholz, N.A., Naegeli, K., Spence, G.D., 2018. Slope failures along the deformation front of the Cascadia margin: linking slide morphology to subduction zone parameters. *Geol. Soc. Lond., Spec. Publ.* 477, 47–67.

<https://doi.org/10.1144/SP477.33>.

- Sammartini, M., Camerlenghi, A., Budillon, F., Insinga, D.D., Zugur, F., Conforti, A., Iori, M., Romeo, R., Tonielli, R., 2019. Open-slope, translational submarine landslide in a tectonically active volcanic continental margin (Licosa submarine landslide, southern Tyrrhenian Sea). In: Lintern, D.G., Mosher, D.C., Moscardelli, L.G., Bobrowsky, P.T., Campbell, C., Chaytor, J.D., Clague, J.J., Georgiopolou, A., Lajeunesse, P., Normandeau, A., Piper, D.J.W., Scherwath, M., Stacey, C., Turmel, D. (Eds.), *Subaqueous Mass Movements and their Consequences: Assessing Geohazards, Environmental Implications and Economic Significance of Subaqueous Landslides*, 477. Geological Society, London, Special Publication, pp. 133–150
- Sassa, K., He, B., Miyagi, T., Strasser, M., Konagai, K., Ostric, M., Setiawan, H., Takara, K., Nagai, O., Yamashiki, Y., Tutumi, S., 2012. A hypothesis of the Senoumi submarine megaslide in Suruga Bay in Japan—based on the undrained dynamic-loading ring shear tests and computer simulation. *Landslides* 9, 439–455.
- Sawyer, D.E., Flemings, P.B., Buttle, J., Mohrig, D., 2012. Mudflow transport behavior and deposit morphology: Role of shear stress to yield strength ratio in subaqueous experiments. *Mar. Geol.* 307–310, 28–39.
- Shiuhara, M., Domitsu, H., Torii, M., Nagahashi, Y., Okuno, M., 2013. Stratigraphy and chronology of Holocene tephras from Ulleungdo volcano (South Korea) distributed in and around the Sea of Japan. *The Quaternary Research (Daiyonki-Kenkyu)* 52, 225–236. <https://doi.org/10.4116/jaqua.52.225>
- Shiuhara, M., Torii, M., Okuno, M., Domitsu, H., Nakamura, T., Kim, K.-H., Moriwaki, H., Oda, M., 2011. Revised stratigraphy of Holocene tephras on Ulleung Island, South Korea, and possible correlatives for the U-Oki tephra. *Quaternary International* 246, 222–232. <https://doi.org/10.1016/j.quaint.2011.08.030>
- Strasser, M., Henry, P., Kanamatsu, T., Thu, M., Moore, G., 2012. Scientific drilling of mass transport deposits in the Nankai Accretionary Wedge: first results from IODP Expedition 333. In: Yamada Y, Kawamura K, Ikehara K, Ogawa Y, Urgeles R, Mosher D, Chaytor J, Strasser M (eds) *Submarine Mass Movements and Their Consequences*. Springer, Dordrecht, pp 671–68.
- Sultan, N., Cochonat, P., Canals, M., Cattaneo, A., Dennielou, B., Haflidason, H., Laberg, J.S., Long, D., Mienert, J., Trincardi, F., Urgeles, R., Vorren, T.O., Wilson, C., 2004. Triggering mechanisms of slope instability processes and sediment failures on continental margins: a geotechnical approach. *Marine Geology* 213(1–4), 291–321. <https://doi.org/10.1016/j.margeo.2004.10.011>.
- Sun, C., Liu, J., You, H., & Nemeth, K., 2017. Tephrostratigraphy of Changbaishan volcano, Northeast China, since the mid-Holocene. *Quaternary Science Reviews* 177, 104–119.
- Tada, R., Irino, T., Ikehara, K. et al. 2018. High-resolution and high-precision correlation of dark and light layers in the Quaternary hemipelagic sediments of the Japan Sea recovered during IODP Expedition 346. *Prog Earth Planet Sci* 5, 19 (2018). <https://doi.org/10.1186/s40645-018-0167-8>
- Tada, R., Murray, R.W., Alvarez Zarikian, C.A., Expedition 346 Scientists, 2015. Proceedings of the Integrated Ocean Drilling Program Volume 346. Integrated Ocean Drilling Program, College Station, TX. <https://doi.org/10.2204/iodp.proc.346.2015>.
- Talling, P.J., Masson, D.G., Sumner, E.J., Malgesini, G., 2012. Subaqueous sediment density flows: Depositional processes and deposit types. *Sedimentology* 59, 1937–2003.
- Tamaki, K., Suyehiro, K., Allan, J., Ingle, J.C., Pisciotto, K., 1992. Tectonic synthesis and implications of Japan Sea ODP drilling, Proc. Ocean Drill. Program Sci. Results, 127–128, 1333–1350.
- Tappin, D.R., Watts, P., McMurtry, G.M., Lafoy, Y., Matsumoto, T., 2002. Prediction of slump

generated tsunamis: The July 17th 1998 Papua New Guinea event. *Science of Tsunami Hazards* 20(4), 222–238.

- Ten Brink, U.S., Geist, E.L., Andrews, B.D., 2006. Size distribution of submarine landslides and its implication to tsunami hazard in Puerto Rico. *Geophys. Res. Lett.* 33, L11307. <https://doi.org/10.1029/2006GL026125>
- Twichell, D.C. Chaytor, J.D., ten Brink, U.S., Buczkowski, B., 2009. Morphology of late Quaternary submarine landslides along the U.S. Atlantic continental margin. *Marine Geology* 264 (1–2),4–15.
- Urgeles, R., Camerlenghi, A., 2013. Submarine landslides of the Mediterranean Sea: trigger mechanisms, dynamics and frequency-magnitude distribution. *J. Geophys. Res. Earth Surf.* 118, 2600–2618.
- Vanneste, M., Mienert, J., Bünz, S., 2006. The Hinlopen Slide: A giant, submarine slope failure on the northern Svalbard margin, Arctic Ocean. *Earth and Planetary Science Letters* 245(1–2), 373–388. <https://doi.org/10.1016/j.epsl.2006.02.045>.
- Watts, P., 2004. Probabilistic predictions of landslide tsunamis off Southern California. *Marine Geology* 203(3–4), 281–301.
- Wells, D., Coppersmith, K., 1994. New empirical relationships among magnitude, rupture length, rupture width, rupture area, and surface displacement. *Bull. Seismol. Soc. Am.* 84 (4), 974–1002.
- White, J.D.L., Houghton, B.F., 2006. Primary volcanoclastic rocks. *Geology* 34 (8), 677–680.
- Wiemer, G., Kopf, A., 2015. Altered marine tephra deposits as potential slope failure planes? *Geo-Marine Letters* 35, 305–314.
- Wiemer, G., Kopf, A., 2017. On the role of volcanic ash deposits as preferential submarine slope failure planes. *Landslides* 14, 223–232.

Core no	Depth (cm)	SiO ₂	Al ₂ O ₃	TiO ₂	Fe ₂ O ₃	MnO	MgO	CaO	Na ₂ O	K ₂ O	P ₂ O ₅
20MAP-P15	30-32	60.81	18.31	0.18	4.14	0.27	0.18	0.97	9.43	5.65	0.06
20MAP-P16	116-119	61.01	18.20	0.30	4.03	0.25	0.35	1.31	8.76	5.70	0.09
20MAP-P16	237-239	61.58	17.67	0.35	4.40	0.19	0.48	1.35	7.91	5.99	0.10
20MAP-P16	383-385	61.68	17.90	0.34	4.16	0.19	0.32	1.30	8.16	5.85	0.10

Table 1: Major elements (wt.%) of the selected tephra layers found in the cores from the ESKP. See figure S1 for the location of the analyzed samples. Normalized to 100%.

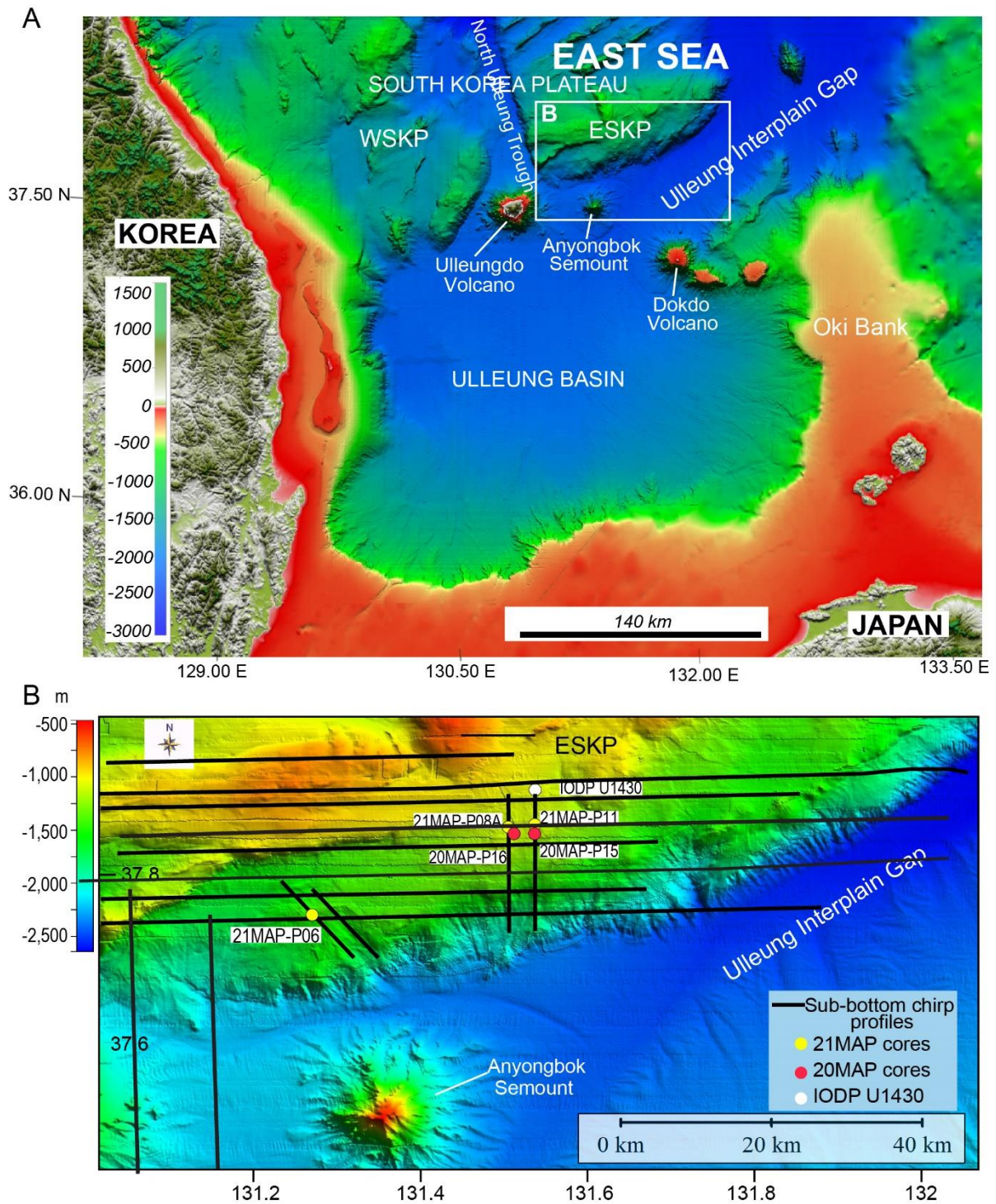


Fig. 1: **A** Bathymetric map of the East Sea showing the major tectonic features including the Ulleung Basin and South Korea Plateau (SKP). The SKP is divided into two physiographic provinces: the Western South Korea Plateau (WSKP) and the Eastern South Korea Plateau (ESKP) which is the focus of our study. **B** Bathymetric map showing the study area and the locations of sub-bottom chirp profiles and the piston cores collected in 2020 and 2021. Also shown is the location of the IODP Expedition 346 drilling site, U1430.

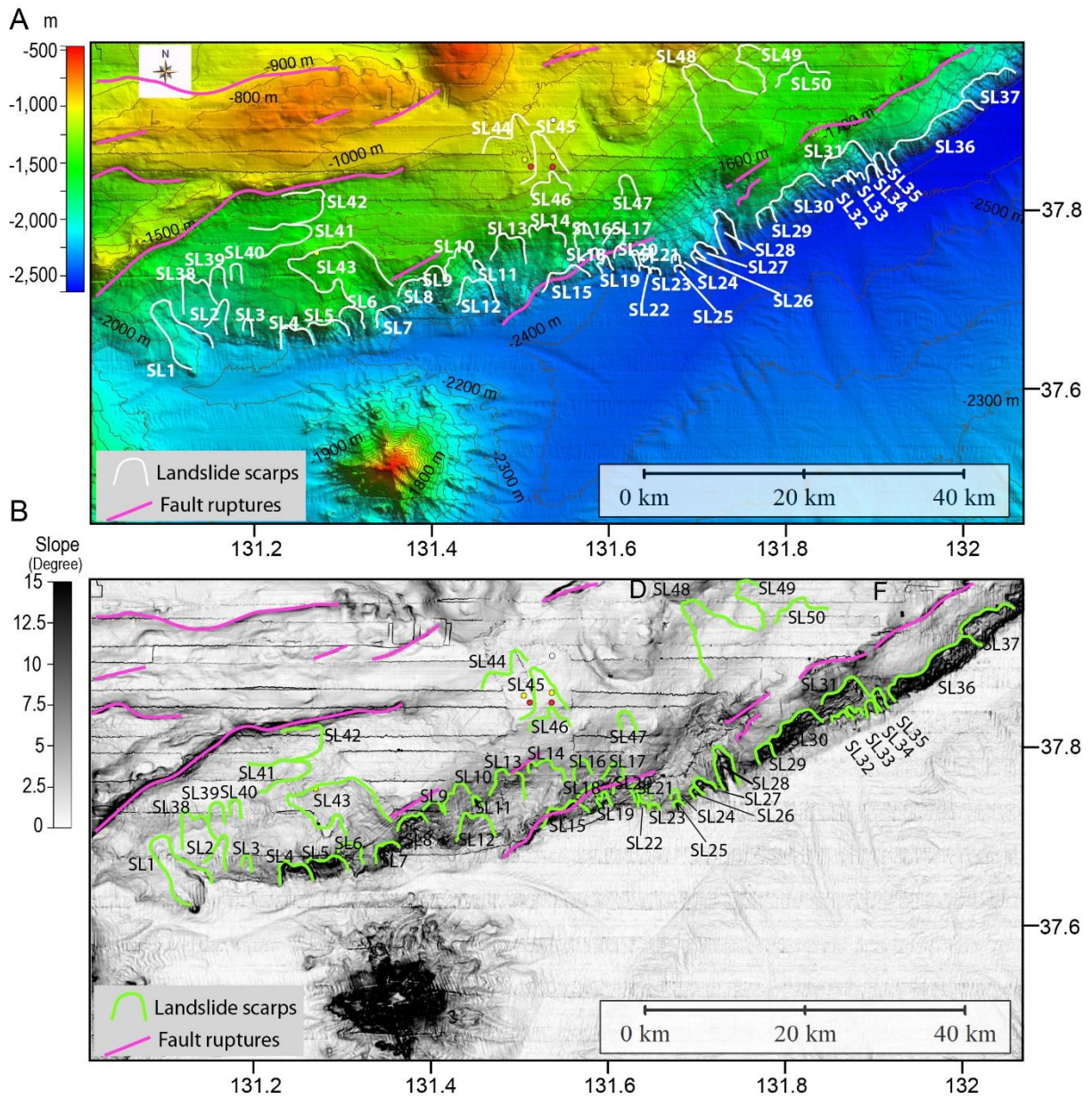


Fig. 2: **A** Multibeam echosounder (MBES) data showing the bathymetry of the study area and the identified submarine landslides (labeled as SL1 to SL50). Surface fault ruptures and the locations of piston cores are also shown. **B** Slope gradient map of A showing the identified landslides and their locations.

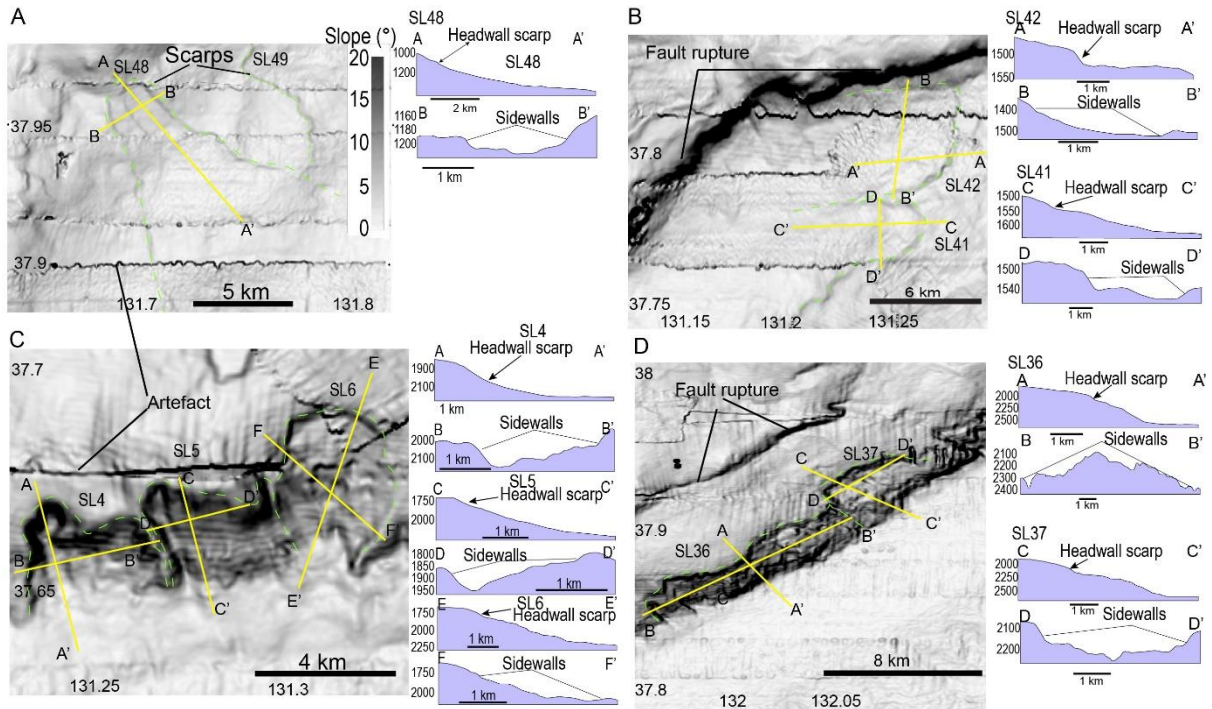


Fig. 3: **A, B** Example of the scarp morphologies in the upper slope showing longer runouts and smaller headwalls with smooth evacuated surfaces. **C, D** Example of the scarps in the lowermost slopes, which have taller headwalls with steep gradients and smaller runouts. The deposits (with toes) in the landslide below the base of the scarps show a blocky surface. Profiles A–A', B–B', C–C', D–D, E–E', and F–F' show cross-sections of landslide scarps and MTDs.

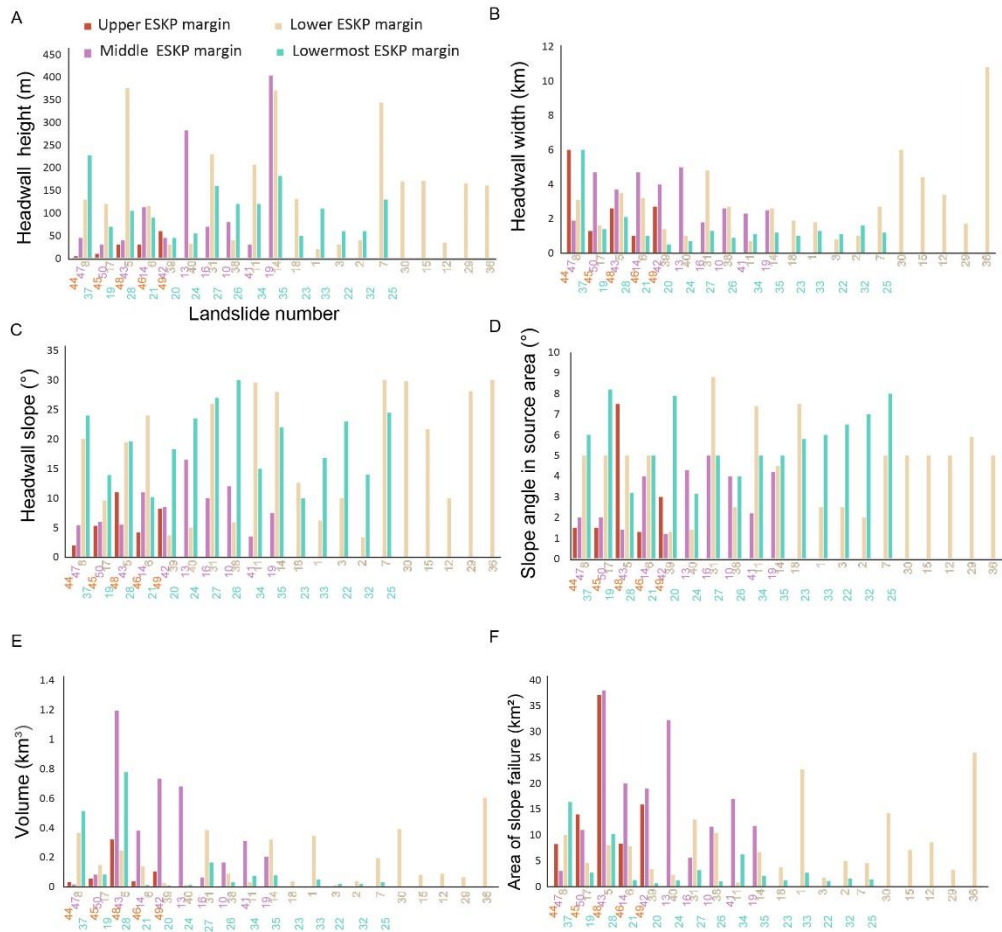


Fig. 4: Morphologic parameters of the 50 submarine landslides identified on the ESKP. **A** Headwall height, **B** headwall width, **C** headwall slope, **D** slope angle in the source area, **E** volume, and **F** area of slope failure. The landslide scarps are 5–400 m high, with an average of 115 m. Headwall widths range from 0.5 km to 11 km, with a mean value of ~2.5 km. The slope angle in the source area and the headwall scarp slopes become steeper towards the lower and lowermost ESKP margin (C), (D).

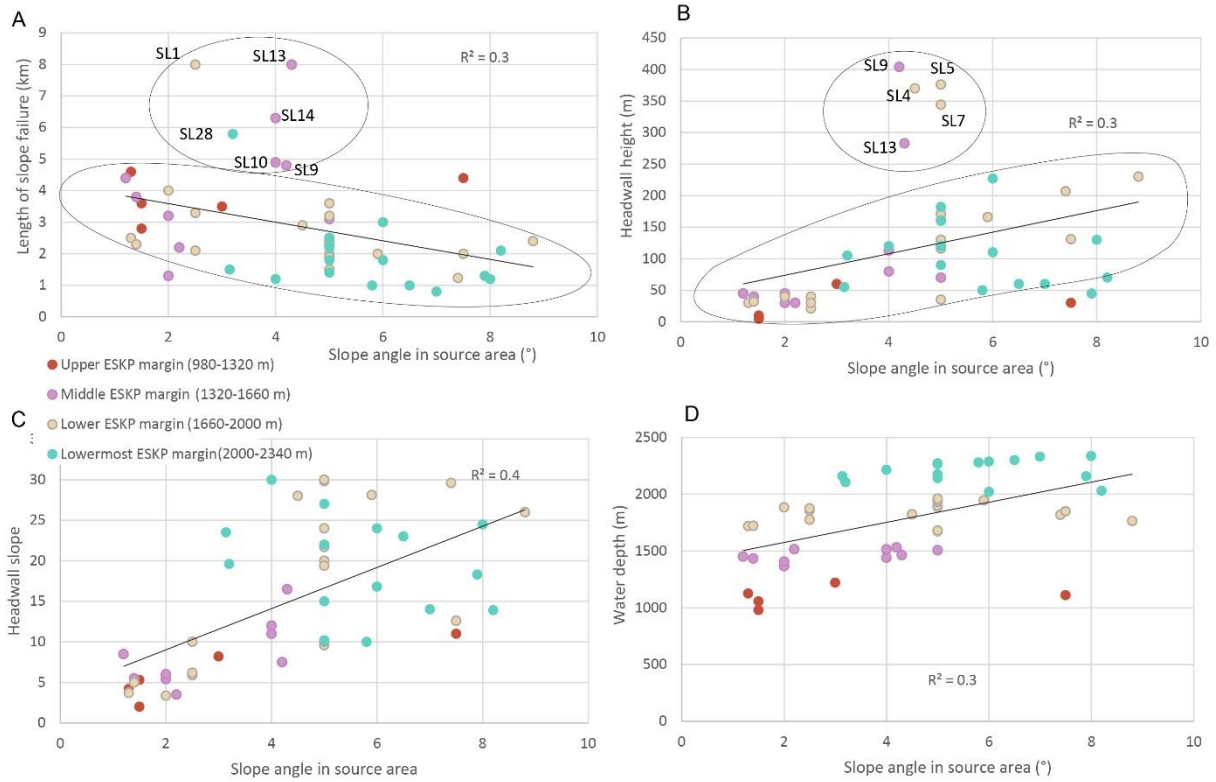


Fig. 5: Relationship between landslide parameters in the upper, middle, lower, and lowermost ESKP margin. **A** Length of slope failure vs. slope angle in the source area, **B** headwall height vs. slope angle in the source area, **C** headwall slope vs. slope angle in the source area, **D** water depth vs. slope angle in the source area.

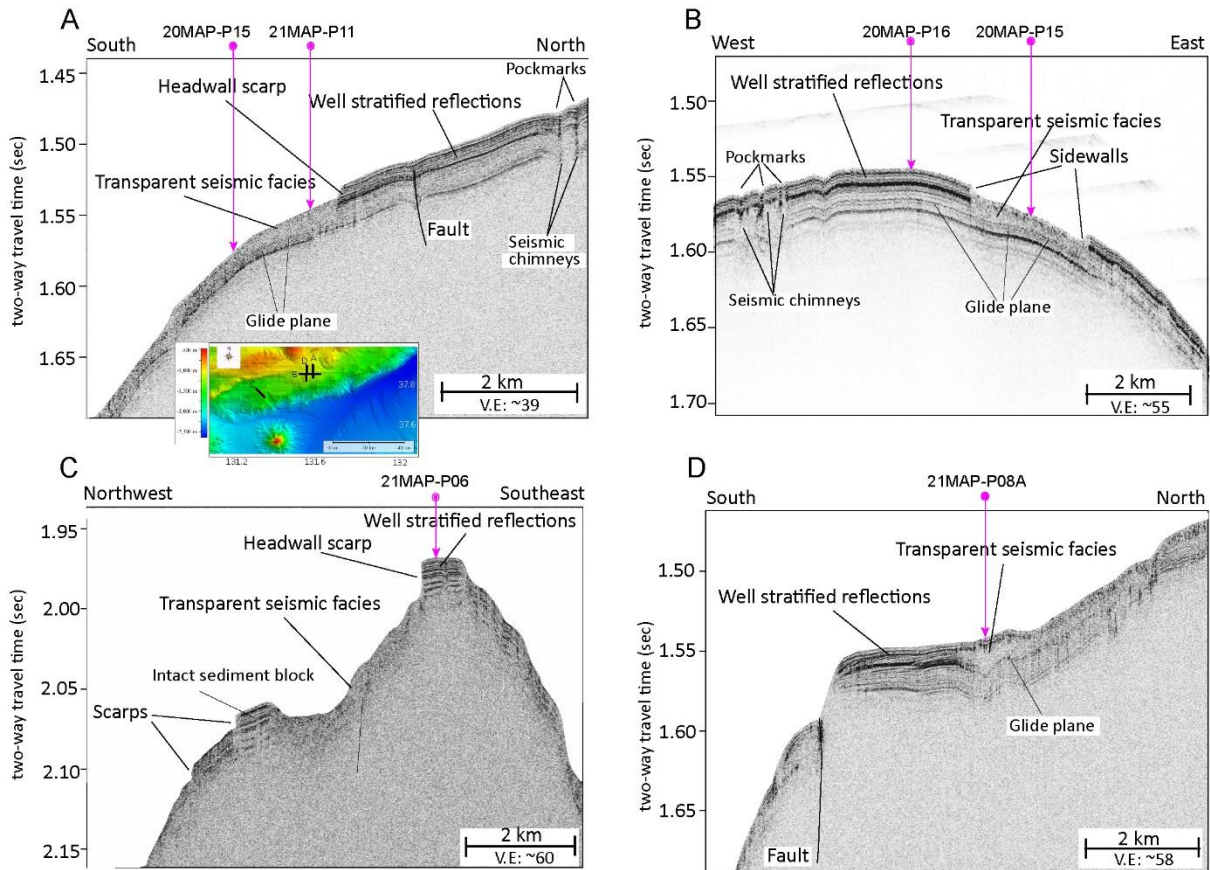


Fig. 6: A–D Subbottom chirp profiles traversing landslide headwall scarps, which show transparent seismic facies interpreted as mass-transport deposits (MTDs). Strata upslope of the scarps are characterized by well-stratified seismic reflections interpreted as hemipelagic sediments interbedded with pumice-rich tephra layers. The glide planes form the base of the MTDs and are characterized by slope-parallel high-amplitude continuous reflections. Also evident on the chirp seismic profiles are the presence of faults and acoustic anomalies such as seismic chimneys and pockmarks adjacent to the scarps. Pink arrows represent the projection of the core locations. **E** The inset MBES map showing locations of all four chirp seismic profiles.

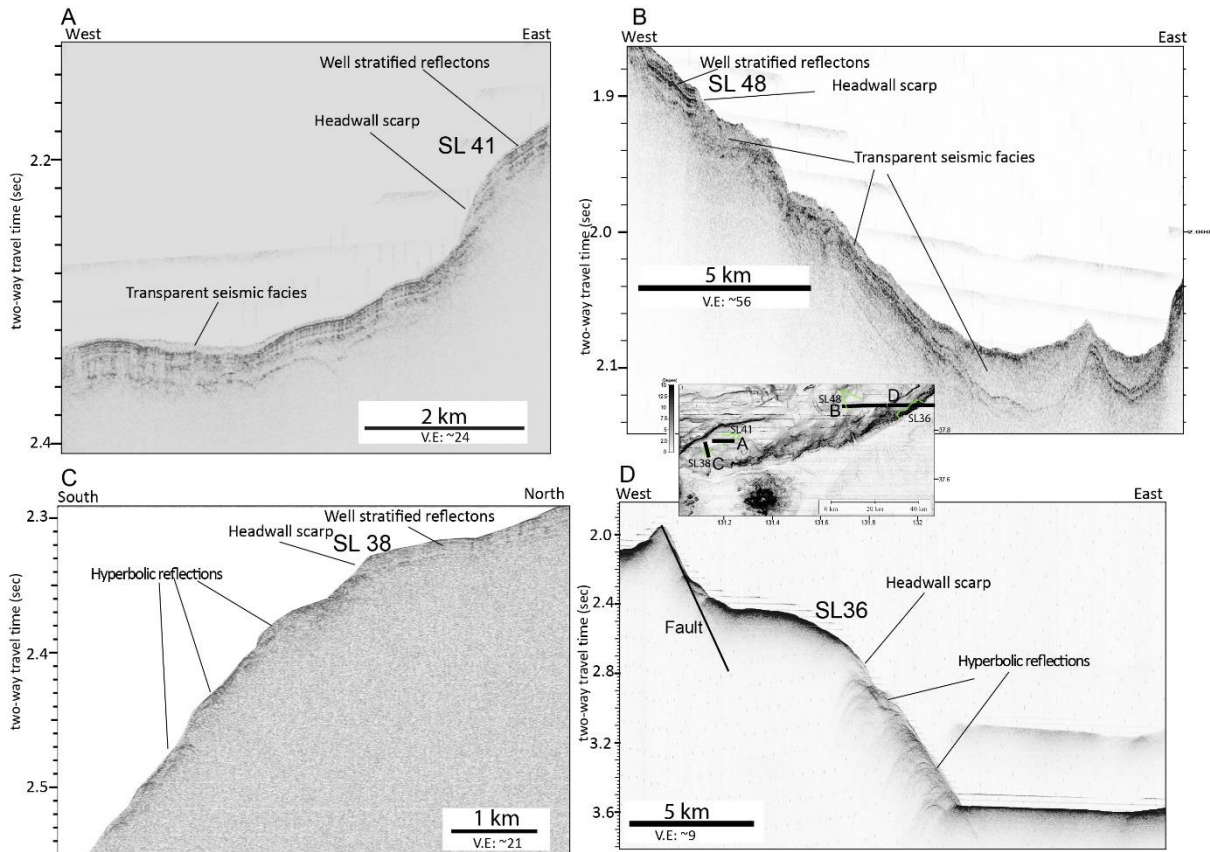


Fig. 7: A–D Chirp seismic profiles traversing SL41, SL48, SL38, and SL36 and displaying headwall scarps. The MTDs on the upper slope (Fig. 7A-B) are characterized by wedge-shaped transparent seismic reflections while those on the lower slope exhibit hyperbolic reflections (Fig. 7C-D). Chirp seismic profile in Figure 7D also shows a prominent seafloor fault immediately above the SL36 headwall scarp.

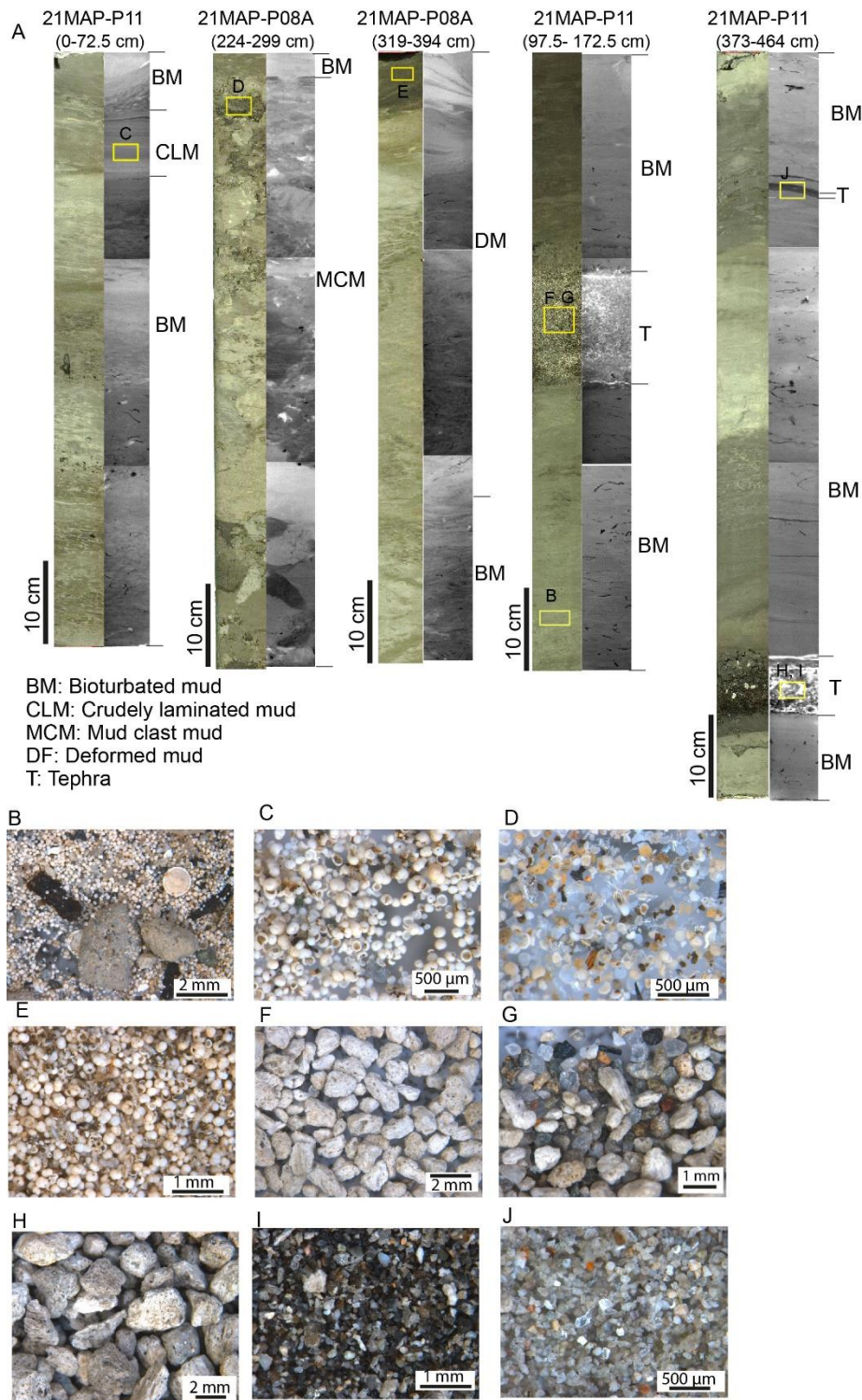


Fig. 8: A Photographs showing representative sedimentary facies identified from the piston cores, including bioturbated mud (BM), crudely laminated mud (CLM), mud-clasts mud (MCM), deformed mud (DM), and tephtras (T). Microscopic images from representative sedimentary facies, with abundant foraminifers **B–E**, abundant pumices **F–H**, abundant volcaniclastic sand/ash to lapilli **H, I**, and thin tephra layer **J**.

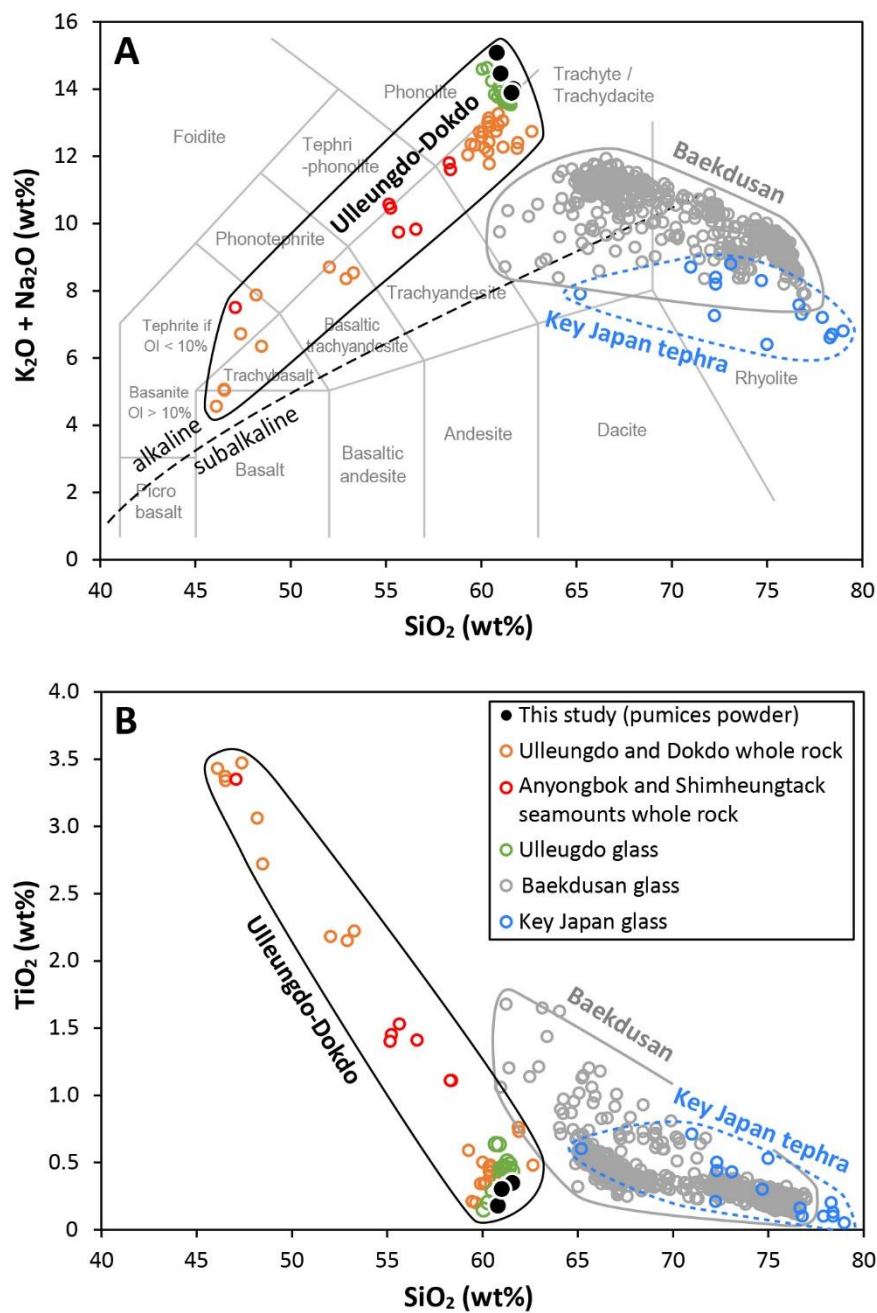


Fig. 9: Geochemistry of pumiceous tephra layers. **A** Total alkali-silica diagram. **B** SiO_2 - TiO_2 diagram. Ulleungdo, Dokdo, Anyongbok, and Shimheungtaek whole rock data are from Choi et al. (2022). Ulleungdo glass is from Shiihara et al. (2011), Baekdusan glass is from Sun et al. (2017), and key Japan glass is from Ikehara (2015) and references therein.

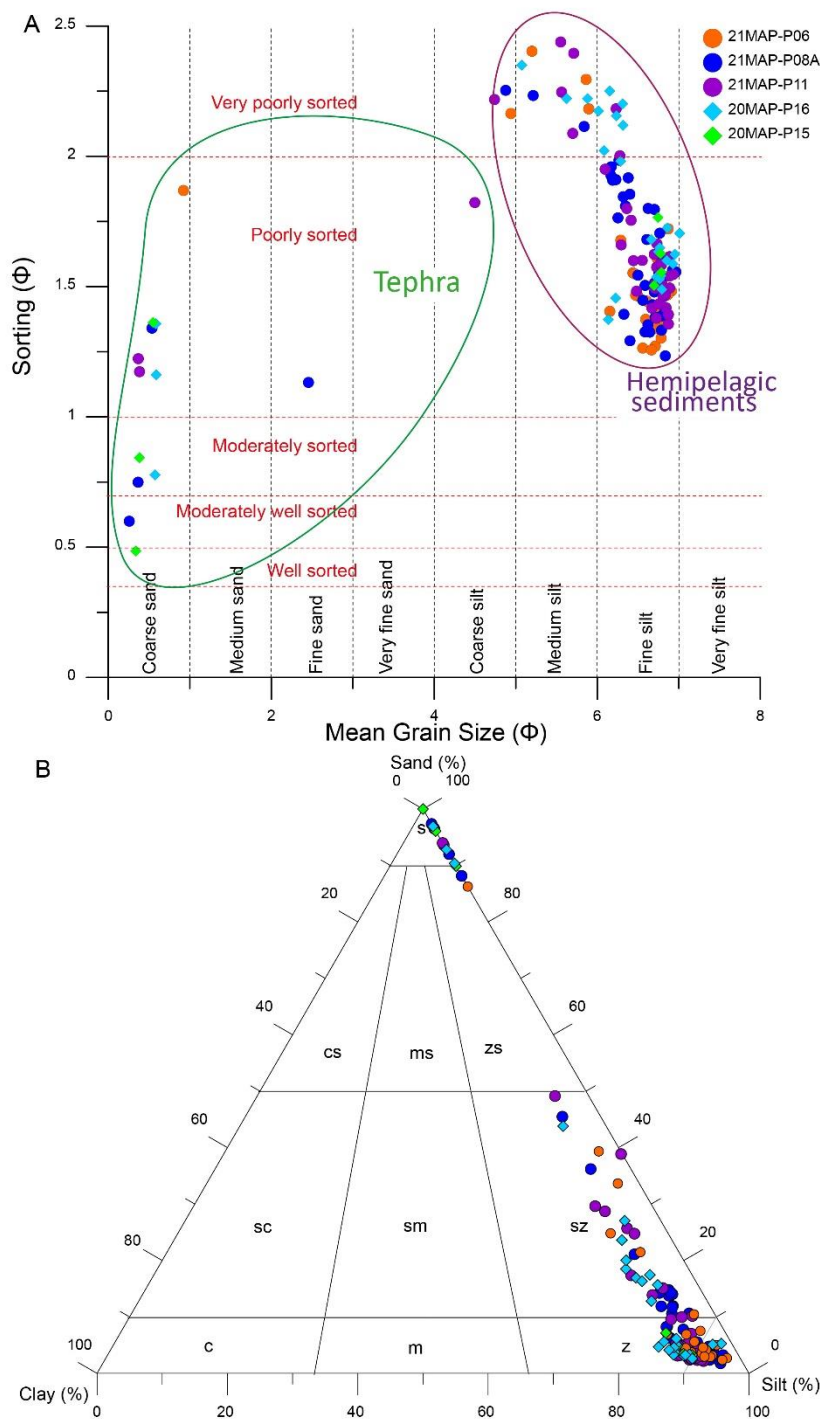


Fig. 10: **A** Sorting vs grain size of the samples recovered from the piston cores. The hemipelagic sediments primarily consist of poorly sorted fine silt whereas the interbedded tephra layers contain poorly sorted to moderately well-sorted coarse sand. **B** Triangular diagram showing the grain-size distribution of sediments (textural classes of Folk, 1954) Notice different sediment types, i.e., the background hemipelagic sediments have silt or sandy silt composition whereas the majority of tephra have sandy composition.

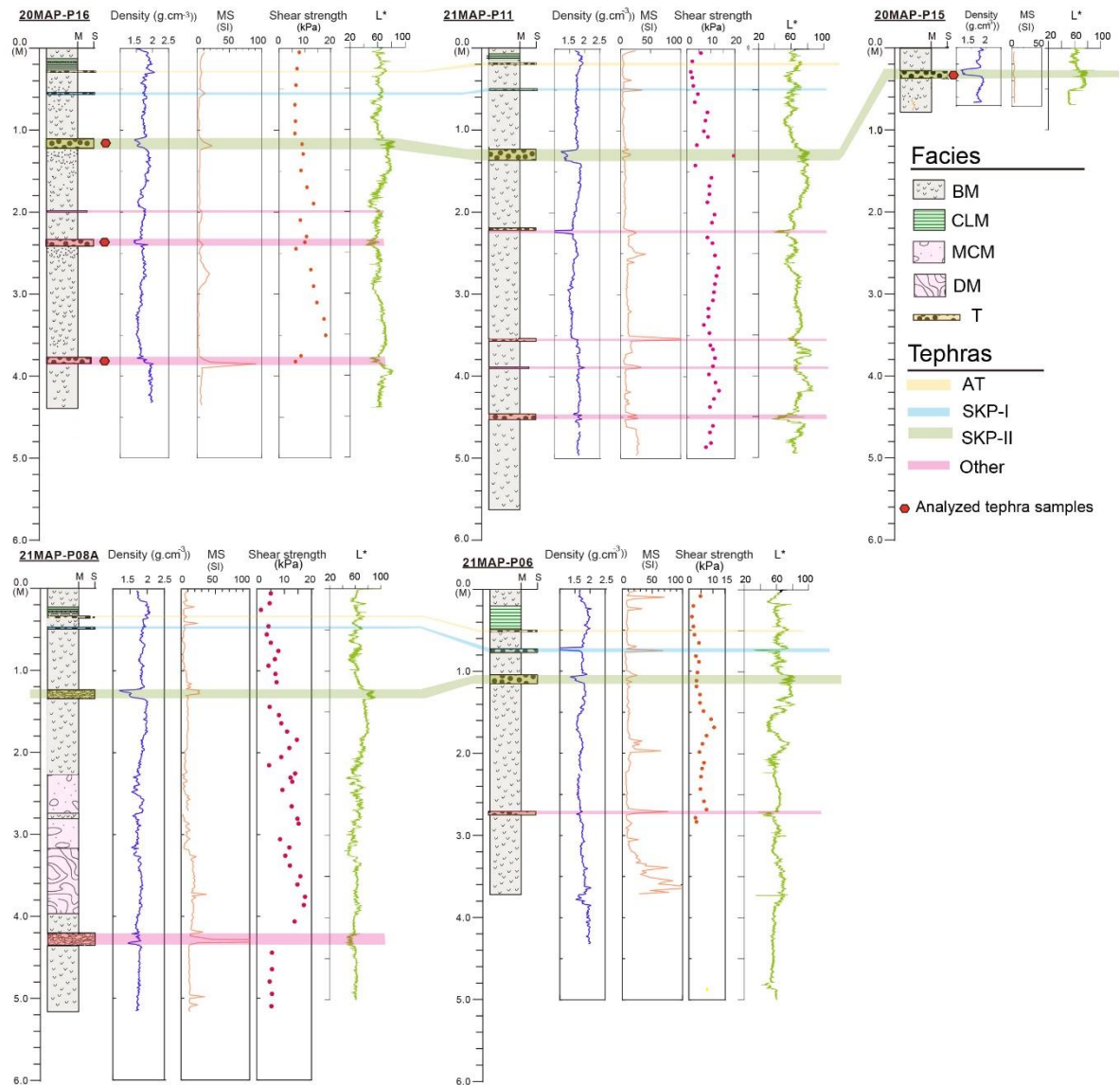


Fig. 11: Physical properties of cores obtained from the ESKP. GRA bulk densities range from a minimum of 1.5 g/cm³ to a maximum of 2 g/cm³. Major decreases in density and increases in magnetic susceptibility (MS) in the cores are associated with tephra layers. Also, not all the tephra layers have a higher MS which would primarily depends on the composition. The high MS layers are most commonly associated with those with magnetite. Layers with non-magnetic black minerals (i.e., pyroxene or amphibole) are not responsible for high MS values. Shear strengths gradually increase with depth; the MTD unit in core P08A shows also higher shear strengths compared to the background hemipelagic sediments. Changes in the L* occur in association with the presence of darker (organic-rich) and lighter (biogenic-rich) sediments.

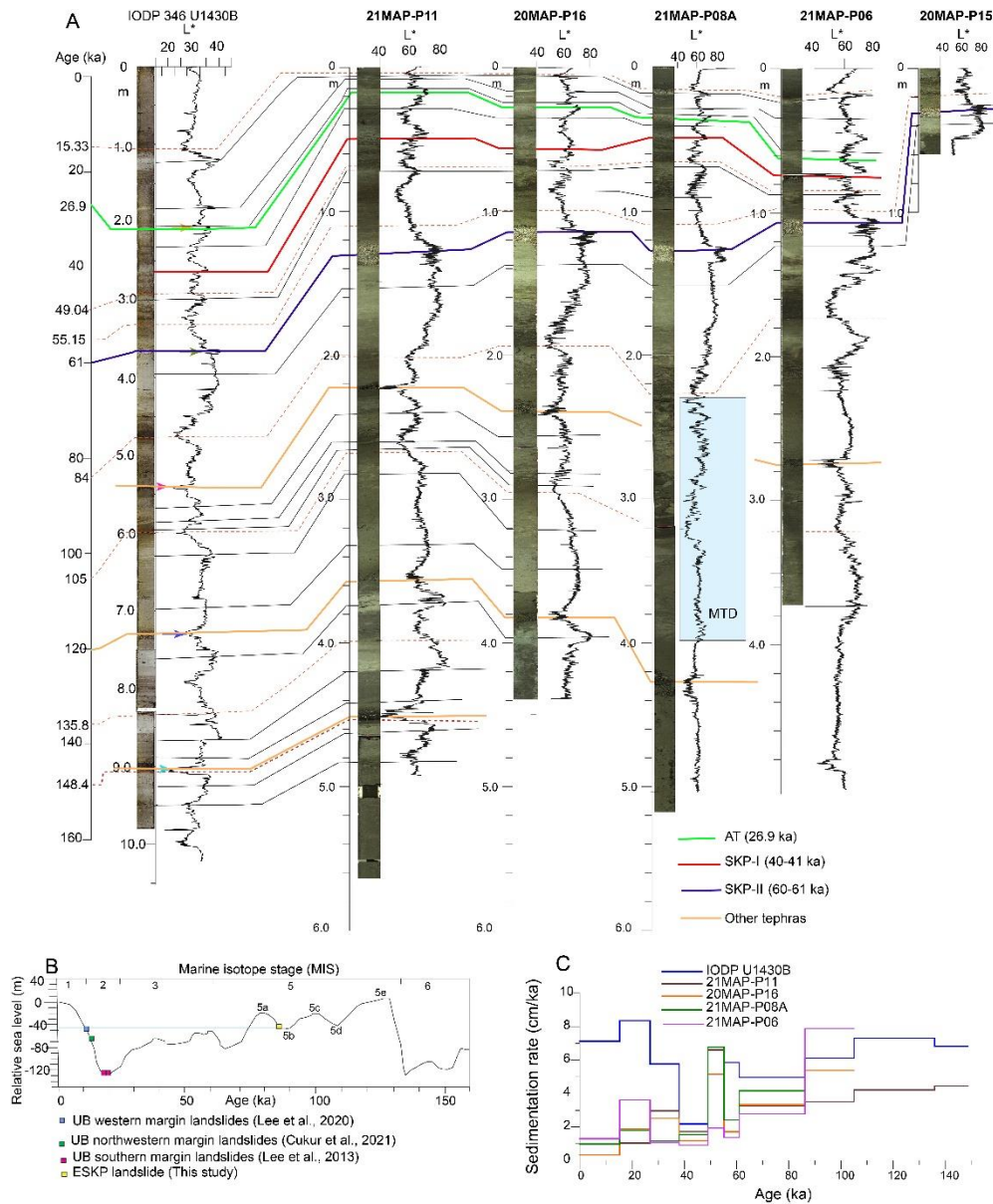


Fig. 12: **A** Correlation of L* between the IODP 346 Site U1430B and 20MAP and 21MAP cores (red dashed lines represent tie points). Arrows mark correlated tephra layers in the cores. The ca. 10 cm thick tephra layer ((SKP-II 60-61 ka; Chun et al., 2007)) layer provides an excellent age marker throughout the cores. **B** Sea-level curve during the Late Pleistocene (after Stanford et al. 2011 and Waelbroeck et al. 2002) with the dated landslide plotted on the curve. The observed landslide occurred around 84 ka ago when the sea level was 70 m lower than the present day. Other landslides which occurred along the margins of the Ulleung Basin (UB) are also plotted **C** Sedimentation rates in the cores; each step corresponds to a correlated interval in (A). Notice that the ESKP margin is characterized by relatively low sedimentation rates (ca. <8 cm/kyr).

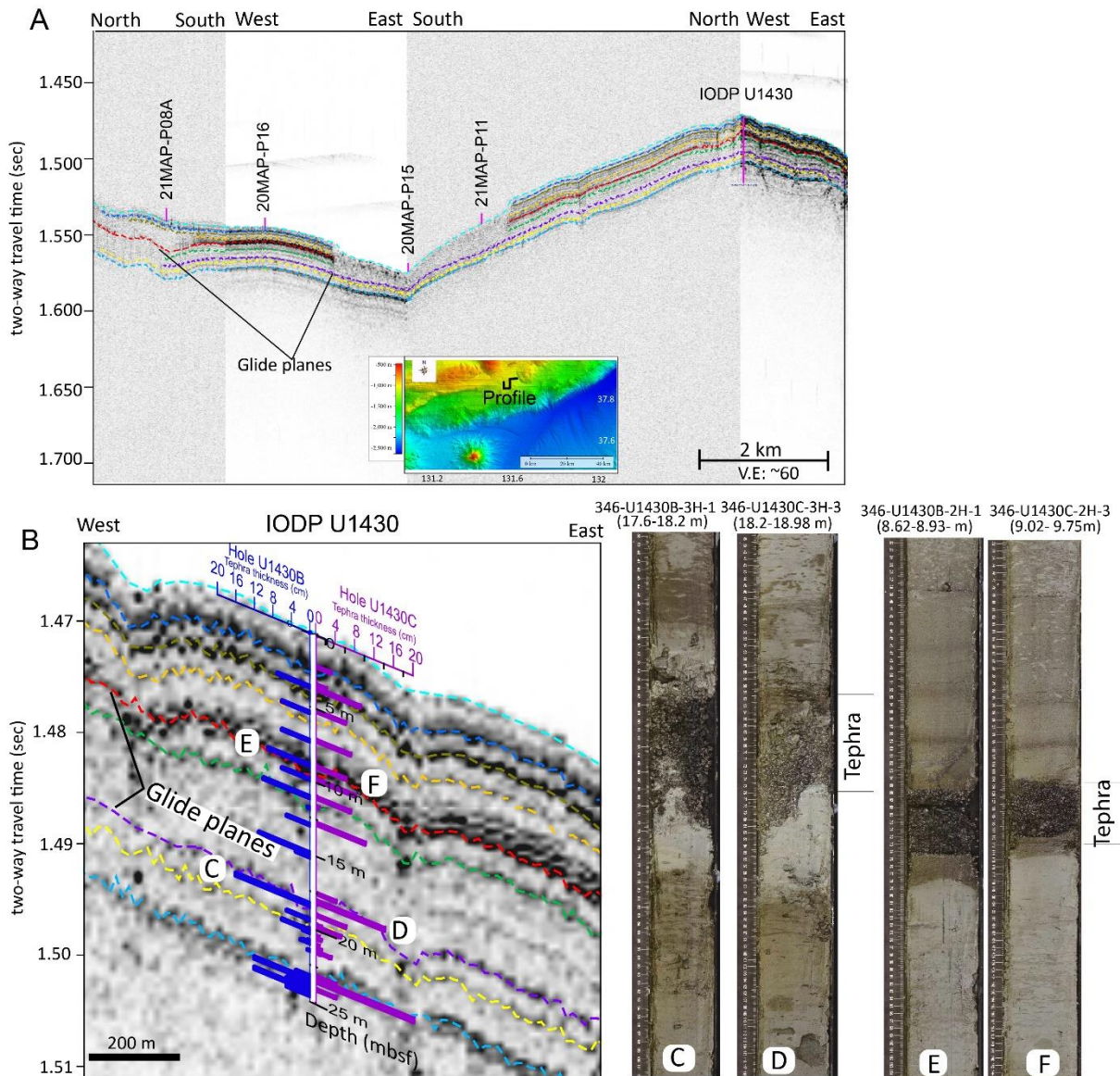


Fig. 13: **A** Correlation of prominent seismic reflectors including the glide planes of the observed landslides (magenta and red horizons) to nearby IODP Site U1430. **B** Close-up sub-bottom chirp profile traversing the IODP Holes U1430B and U1430C revealing a good correlation between the occurrence of thick tephra layers and some of the glide planes (i.e., magenta and red horizons). **C, D, E, F** Core photographs from IODP Holes U1430B and U1430C showing thick tephra layers that are correlated to failure planes of the observed landslides (magenta and red horizon).

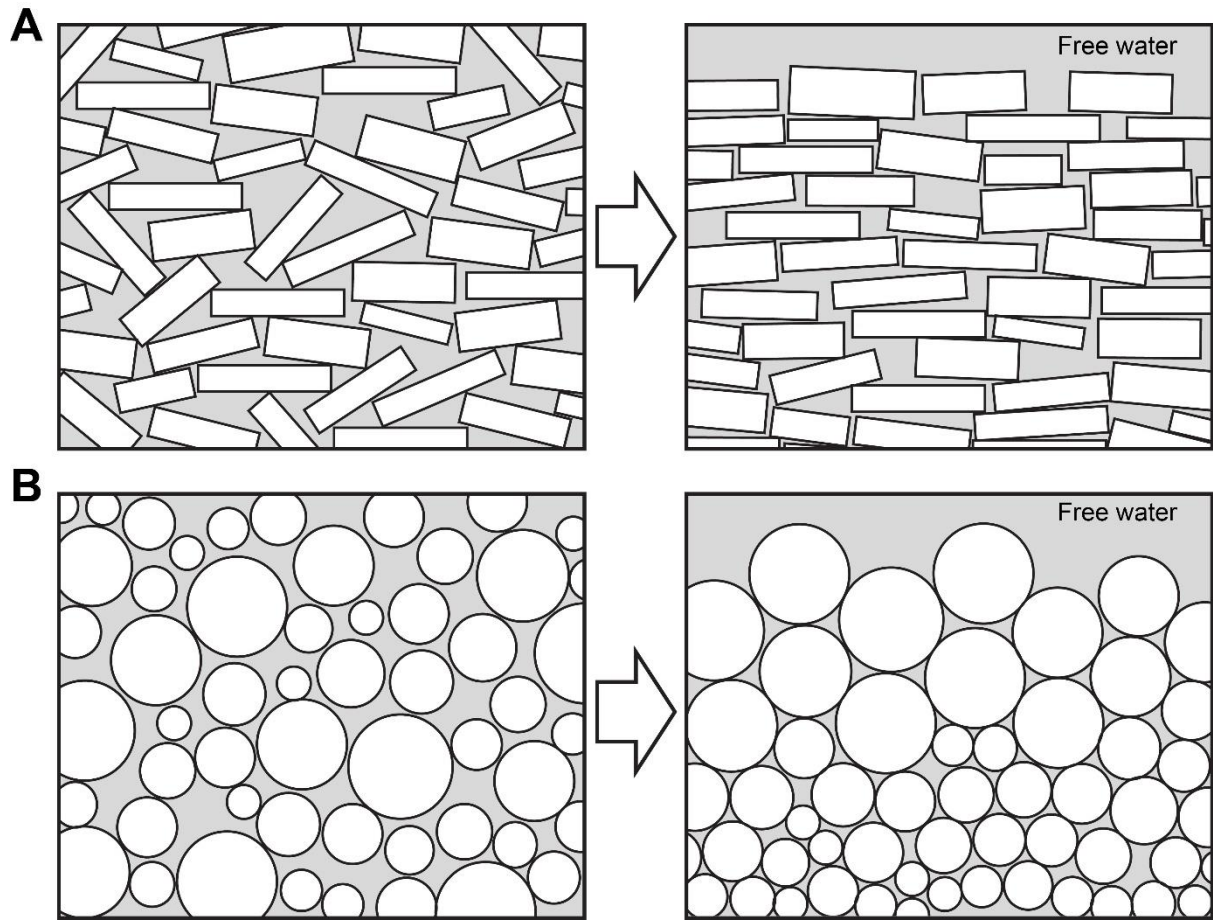


Fig. 14: Cartoons showing granular convection hypothesis with the reorientation of asymmetrical particles **A**, and symmetrical particles **B**. The smaller particles percolate between the larger particles, resulting in an increase in compaction and a reduction of pore spaces. Consequently, the reorganization of these particles creates a free water layer at the top.

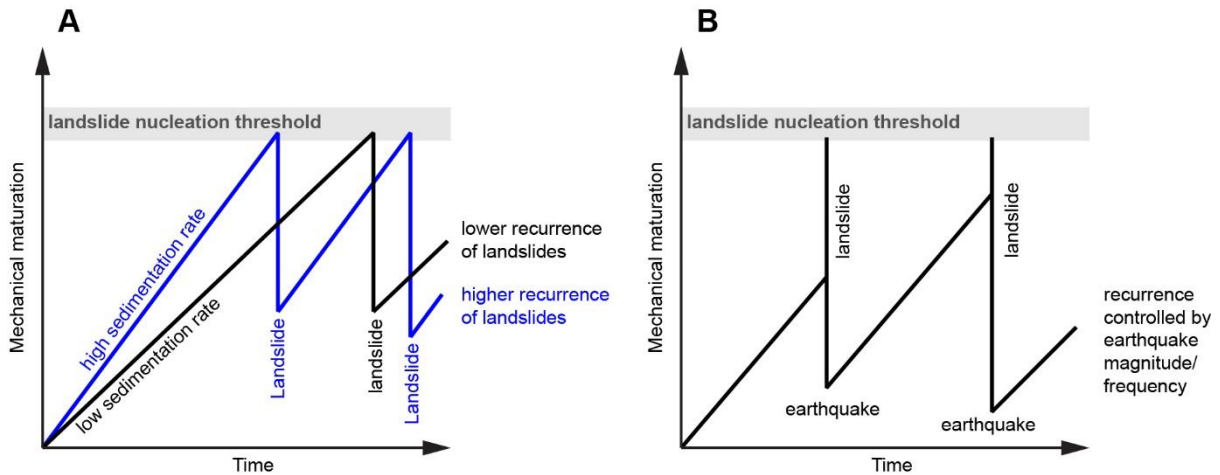
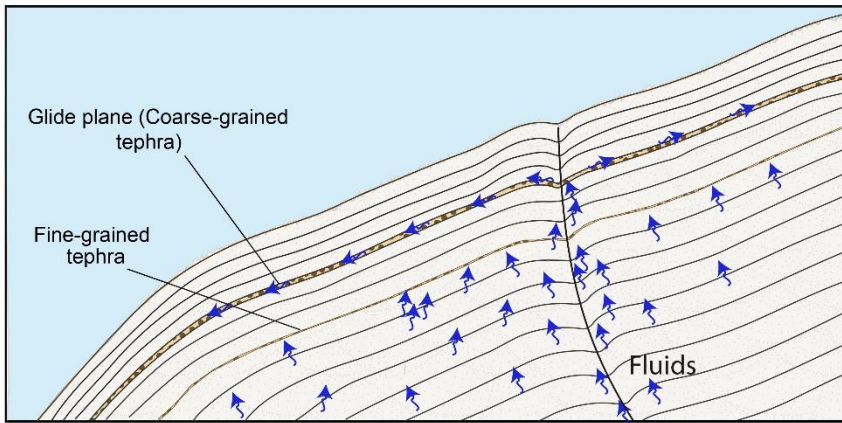
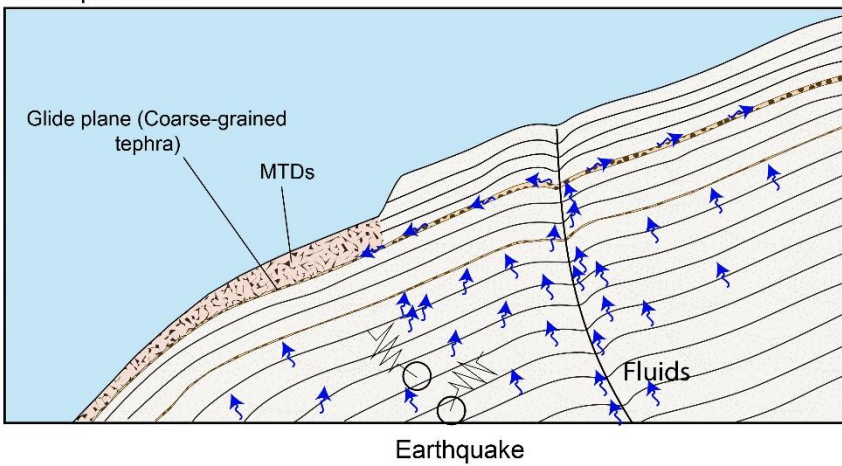


Fig. 15: Model of mechanical maturation for the nucleation of submarine landslides showing possible links between (i) internal and external factors that control landslide nucleation and (ii) temporal patterns of landslides in a basin. **A** Continuous maturation is controlled by slow-paced internal processes such as sediment compaction and/or long-term build-up of pore pressure. These can be indirectly linked to external factors such as the rate of sedimentation or sea level change. A landslide is triggered when the mechanical maturation reaches a threshold value that is characteristic of the composition (mineralogy and geochemistry) of the sedimentary deposits as well as the seafloor morphology. Landslides are accompanied by local decrease of mechanical maturation (e.g., release of pore pressure). **B** Discontinuous maturation is similar to (A) but affected by short-term, high-magnitude external processes such as earthquakes and faulting, that can significantly increase the recurrence of landslides in a basin. (A) and (B) are not mutually exclusive, but characterising the spatial and temporal patterns of landslides can provide insight into the main controls of landslide nucleation in a given basin, especially if cycles or pulses of landslide formation are identified.

A Pre-failure



B Slope failure



C Post-failure

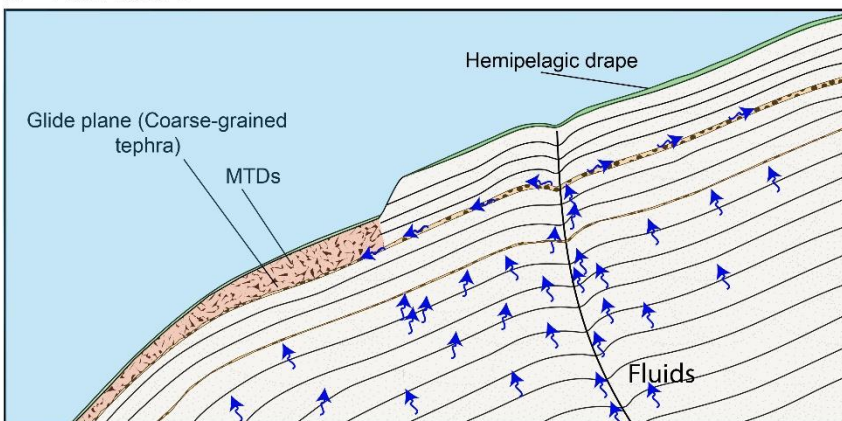


Fig. 16: Schematic diagrams showing the development of submarine landslides on the EKSP. **A** Fluids migrate upslope through faults or fractures and accumulate along the thick coarse-grained tephra layers. The glide planes develop along these tephra layers because they are coarser and more susceptible to allow the fluid to flow through them. **B** Strong earthquakes triggered by tectonic activity create additional loading and trigger liquefaction along these pressurized tephra layers and trigger submarine landslides. **C** The margin becomes stable and hemipelagic sedimentation dominates the study area.

Supplementary Figures – supplementary tables available online or upon request

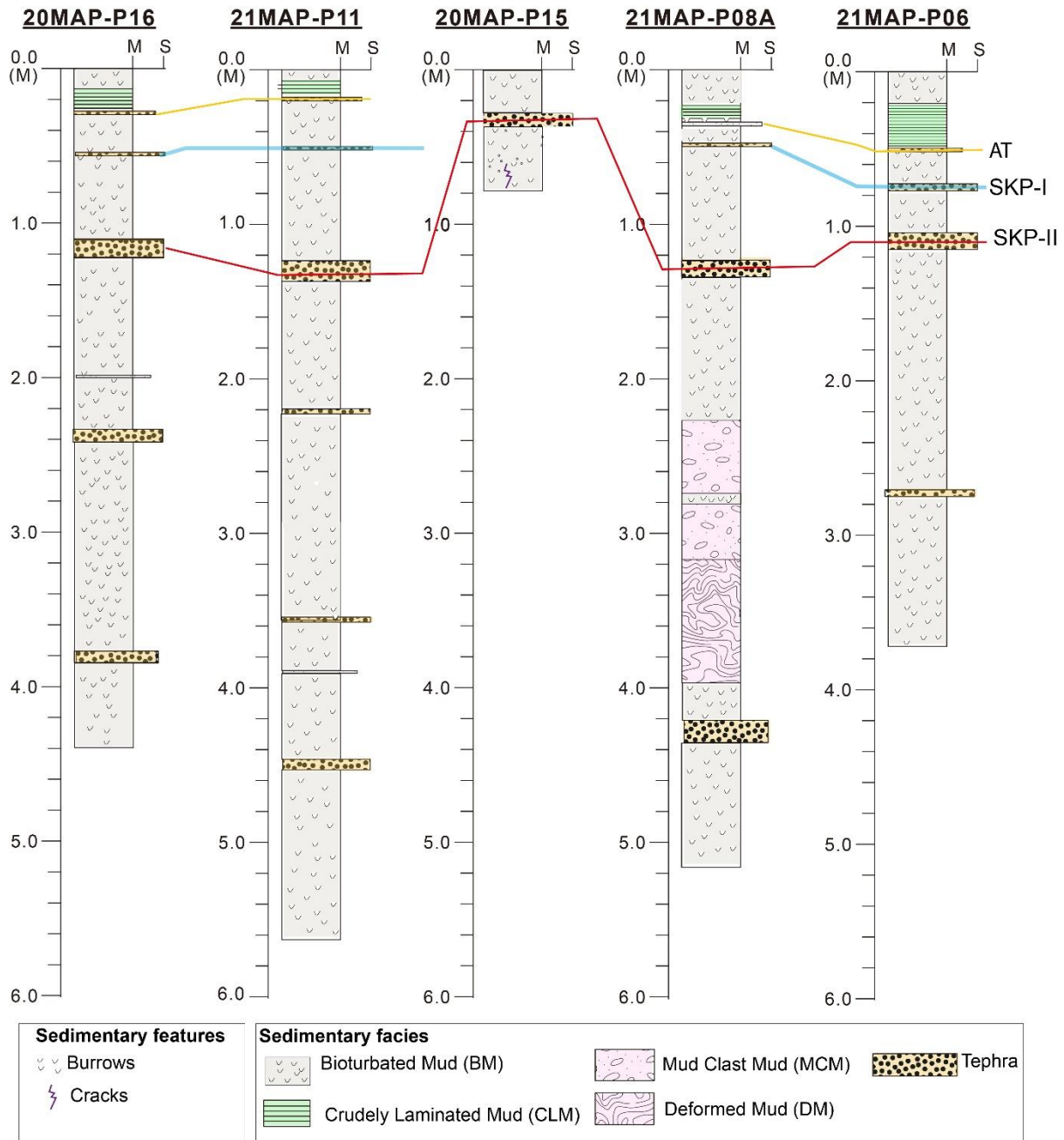


Fig. S1: Columnar occurrence of sedimentary facies identified across the piston cores. The sediments consist mostly of bioturbated mud (BM) with frequent alternations of tephra layers. Crudely laminated mud (CLM) facies occur at the uppermost part of the core sediments. Mud clast mud (MCM) and deformed mud (DM) occur in core P08A and are underlain and overlain by BM facies. BM and CLM facies are interpreted as deposits of hemipelagic settling, whereas MCM and DM are interpreted as mass-transport deposits (MTDs). Thick lines represent the tie line of the AT, SKP-I, and SKP-II tephra.

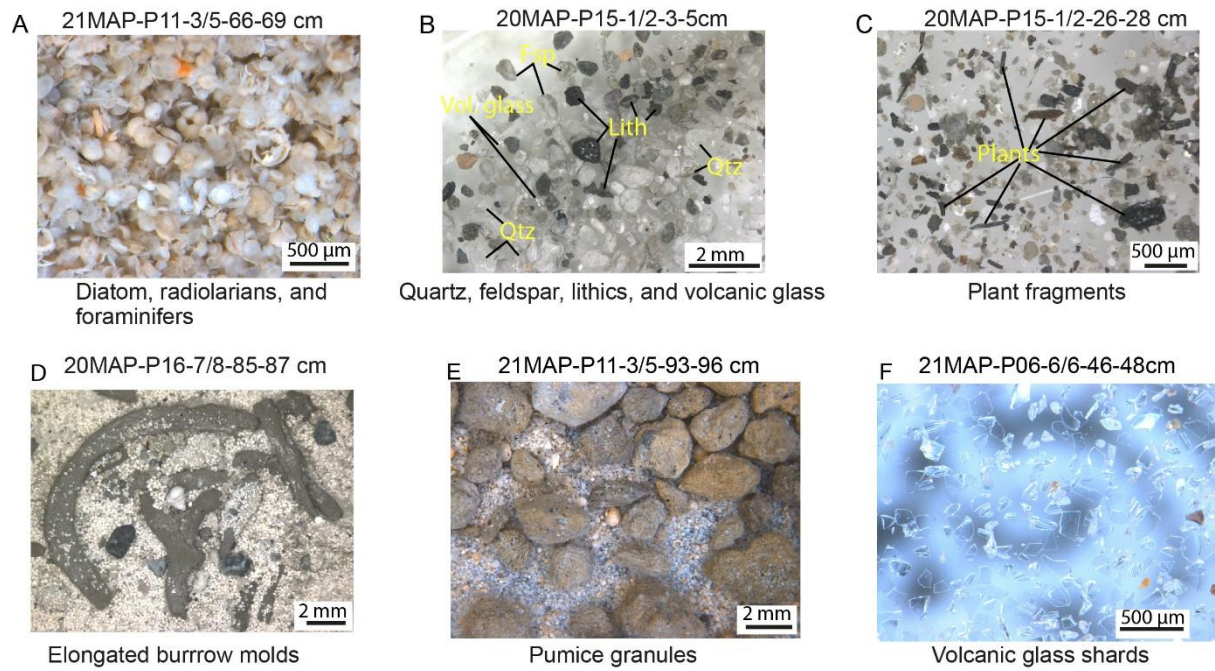


Fig. S2: Photographs of common siliciclastic, biogenic, organic, and volcanoclastic particles recovered from the piston cores. **A** Diatom, radiolarians, and foraminifers. **B** Quartz (Qtz) feldspar (Fsp), lithics (Lith.), and volcanic glass shards (Vol. glass). **C** Plant fragments. **D** Elongated burrow molds. **E** Pumice granules. **F** Volcanic glass shards.

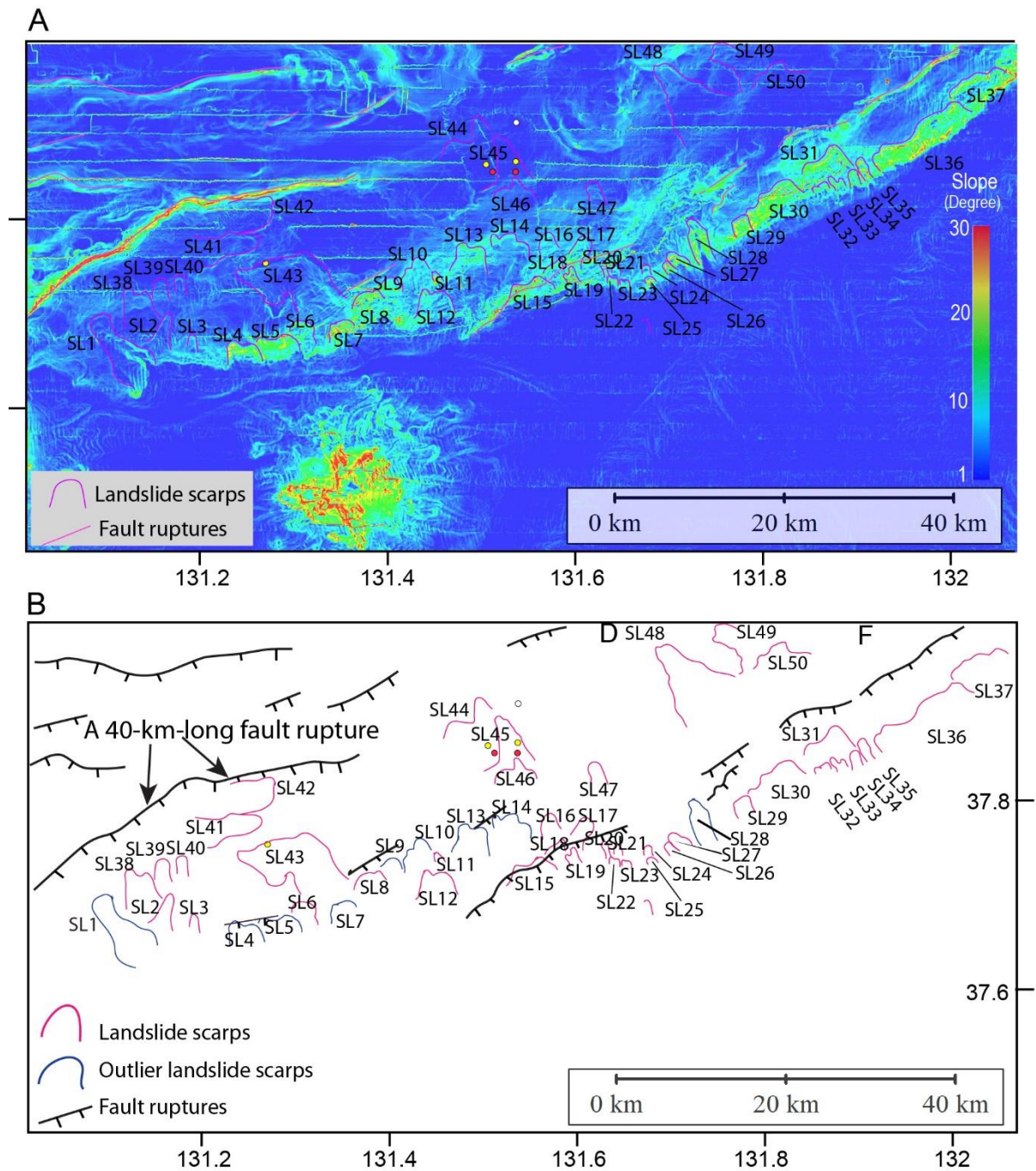


Fig. S3: **A** Slope gradient map of the study area. The gradient of the slope increases towards to lower slope, reaching up to 30°. **B** Structural map showing the location of major faults and submarine landslide scarps. Notice that the outlier landslides (marked as blue) are located close to the major faults.